

Doppler Bias: Impact of Peculiar Velocities on Color Selection and the Large Scale Structure of Galaxy Surveys

Batia Friedman-Shaw,^{a,b,c,1} Alex Krolewski,^{c,b,a,*} Matteo Foglieni,^d and Niayesh Afshordi^{a,b,c}

^aPerimeter Institute for Theoretical Physics,
31 Caroline Street North, Waterloo, Ontario, N2L 2Y5, Canada

^bDepartment of Physics and Astronomy, University of Waterloo
200 University Avenue West, Waterloo, ON, N2L 3G1, Canada

^cWaterloo Centre for Astrophysics, University of Waterloo
200 University Avenue West, Waterloo, ON N2L 3G1, Canada

*CITA National Fellow

^dLeibniz Supercomputing Centre (LRZ), Boltzmannstraße 1, 85748 Garching bei München, Germany

Abstract. Light cone selection effects on cosmic observables must be precisely accounted for in the next generation of surveys, including the Dark Energy Spectroscopic Instrument (DESI) survey. This will allow us to correctly model the data and extract subtle shifts from general-relativistic effects. We examine the effects of peculiar velocities on color selection in spectroscopic galaxy surveys, with a focus on their implications for the galaxy clustering dipole $P_1(k)$. Using DESI Emission Line Galaxy (ELG) targets, we show that peculiar velocities can shift spectral emission features into or out of filter bands, modifying galaxy colors and thereby changing galaxy selection. This phenomenon mimics the effect of evolution bias, and we refer to it as the Doppler bias, b_D . The Doppler bias is of comparable size to the evolution bias at $0.8 < z < 1$, where it is largest. This enhances the ELG-LRG (Luminous Red Galaxy) cross-correlation dipole by 15–30%. This could be detectable at the $\sim 4\sigma$ level for the full DESI survey. Additionally, we found that our b_D estimate is impacted by the incompleteness of the parent ELG sample. Therefore, this work highlights the essential need for careful consideration of spectral-dependent biases caused by peculiar velocities during the selection phase of galaxy surveys, to enable unbiased analyses.

¹Corresponding author.

Contents

1	Introduction	1
2	Theory	3
2.1	Impact of the Doppler shift on the observed galaxy power spectrum	3
2.2	Synthetic sample approach to measuring the Doppler bias	5
2.3	Power Spectrum Dipole Calculation	8
3	DESI Emission Line Galaxy selection	8
4	Measuring the Doppler bias	11
4.1	Creating the synthetic sample at each redshift	11
4.2	Measuring synthetic magnitudes and redshifting them	12
4.3	Measuring the change in number of ELGs	14
4.4	Doppler bias measurement	15
5	Linear bias, magnification bias and evolution bias	18
5.1	Linear bias	18
5.2	Magnification bias	18
5.3	Evolution bias	20
6	Impact on two-point statistics	21
7	Conclusion and Future Prospects	25
8	Acknowledgements	26

1 Introduction

We aim to learn about cosmology from the Gaussian linear matter field, but we instead observe the redshift-space distribution of biased tracers (galaxies), which inhabit the evolved, highly nonlinear density field. On large scales, most of the cosmological information is contained in the two-point statistics – the power spectrum or the correlation function – which are very well understood theoretically on linear and quasilinear scales. On large scales (i.e. not including complications from nonlinearities and higher-order bias), the dominant contributor to the observed galaxy density, beyond the real-space density itself, are the peculiar velocities through redshift-space distortions (RSD) [1]. There are a number of other sub-leading contributions, generally termed relativistic effects, which have been extensively studied, especially recently as galaxy surveys reach unprecedented precision [2–5]. These include Doppler effects, magnification bias, gravitational redshift, and the integrated Sachs-Wolfe effect. These additional effects offer a rich laboratory to test gravity and dark matter interactions on large scales [6–10]. Additionally, relativistic effects have a similar scale dependence to the large-scale scale-dependent bias induced by local primordial non-Gaussianities (PNG) [11–16]. Therefore, it is increasingly important to capture relativistic effects in order to better constrain local PNG. In the redshift-space galaxy density field, the relativistic terms are suppressed relative to the dominant matter density, lensing, and RSD components by at least one power

of \mathcal{H}/k , where $\mathcal{H} = aH$ is the comoving Hubble parameter (as described in detail in Section 2.1 below). When computing $P(k) = \langle \delta_k \delta_k^* \rangle$, the peculiar velocity terms are therefore suppressed by a factor of $(\mathcal{H}/k)^2$. The density-velocity cross-terms are imaginary in Fourier space, and thus cancel when multiplying δ_k by its conjugate δ_k^* . However, if we instead consider the cross-correlation of two tracers with different linear biases b_A and b_B , there is a residual imaginary cross-term $\propto (b_B - b_A)\mathcal{H}/k$ [17, 18]. When computing the standard Legendre multipole moments of the power spectrum, this imaginary term generates a nonzero clustering dipole. Since the standard contributions to this dipole are zero, the multi-tracer dipole offers an ideal opportunity to study relativistic effects.

The amplitude of the Doppler terms (and thus, the clustering dipole) depends on astrophysical bias parameters as well as the cosmological contributions. The clustering bias has been extensively studied [19]; the large-scale contributions from beyond-linear-bias terms are suppressed (in a standard Λ CDM cosmology with Gaussian initial conditions) and we will therefore only consider linear bias in this work (though see [5, 20, 21] for interactions between higher-order clustering bias and relativistic terms on quasi-linear scales). The magnification bias describes the response of galaxy number counts to a uniform magnification (e.g. from gravitational lensing or Doppler effects). It can be straightforwardly measured using the faint-end slope of the luminosity function for a simple selection with a one-band flux limit [22]. Measuring the magnification bias is more involved for realistic color-selected galaxy samples [23, 24], but it is nevertheless a straightforward measurement once the galaxy selection function is defined. Finally, the evolution bias defines the response of the comoving galaxy number density to a peculiar velocity shift, and is nonzero if the underlying number density changes as a function of redshift. This can arise, e.g. from mergers in a sample of halos or from mergers or evolution in the underlying galaxy sample [25]. In a galaxy sample selected into a redshift bin, peculiar velocities move galaxies into and out of the sample across the redshift bin boundary. If the galaxy number density changes in redshift, galaxies moving in one direction will be favored, creating a clustering dipole.

Previous derivations of the evolution bias have considered simple situations, e.g. a single-band flux cut or line luminosity limit in [25]. However, a realistic galaxy selection function leads to a more complicated impact of peculiar velocities on the galaxy sample. We consider a spectroscopic survey, where galaxies are targeted based on their fluxes in multiple broad bands, then kept in the sample if spectroscopically confirmed to lie in the correct redshift range. Thus, in addition to perturbing the observed redshift away from the true redshift, peculiar velocities also modify the broad-band fluxes by shifting the galaxy spectrum. This can also affect galaxy number counts by shifting galaxies into, or out of, the initial color selection box. Although this may be a small effect, it can be enhanced if the galaxy flux is dominated by one or a few narrow emission lines, e.g. the case with Emission Line Galaxies (ELGs).

We study this effect of peculiar velocities impacting the color selection of galaxies, which we call the Doppler bias, in detail for a particular set of Emission Line Galaxies following the DESI [26] ELG target selection [27]. We build on the work of [25], replacing the assumption of a global, redshift-dependent K -correction with the full diversity of observed galaxy spectra; and using a multi-band galaxy selection rather than a single flux cut.¹ We show that, for

¹A similar method was applied to estimate the impact of peculiar velocities on the clustering dipole of BOSS LRGs in [28]. This paper directly measured the number of galaxies which scatter across the flux boundary using peculiar velocities estimated by reconstruction, without ever quoting a value for the evolution bias. On the other hand, we measure the change in evolution bias to better connect to the theory in [2, 3, 5, 29].

the DESI ELG sample, the Doppler bias is similar in magnitude to the evolution bias from the change in comoving number density, and thus needs to be considered to accurately model relativistic effects. This effect will be increasingly important for future work, since ELG samples are increasingly favored for high-redshift galaxy surveys (H α for Euclid [30] and Roman [31]; Lyman Alpha Emitters for DESI-II [32] and MegaMapper [33]).

We organize this paper as follows. Section 2 is an overview of the theory describing the impact of relativistic effects on galaxy number counts, and provides an overview of our synthetic-sample approach to measuring the Doppler bias. Section 3 describes the details of the DESI data and galaxy selection. Section 4 details our measurement of the Doppler bias, while Section 5 presents measurements of the magnification bias and evolution bias. Finally, we show the impact on galaxy clustering in Section 6. Lastly, we provide concluding remarks in Section 7.

Unless noted otherwise, we set the speed of light $c = 1$ and use $h^{-1}\text{Mpc}$ as units of both space and time.

2 Theory

2.1 Impact of the Doppler shift on the observed galaxy power spectrum

In linear theory (including relativistic corrections), the galaxy number counts Δ_g , selected only by a *bolometric* flux cut, can be related to the matter overdensity δ_m and the line-of-sight velocity v_{\parallel} [2, 34]

$$\begin{aligned} \Delta_g = & \left\{ b_1 \delta_m + \mathcal{H}^{-1} \partial_r v_{\parallel} \right\} + \left\{ \frac{5s - 2}{2} \int_0^{\chi} d\chi' \frac{\chi - \chi'}{\chi \chi'} \Delta_{\Omega}(\Psi + \Phi) \right\} \\ & + \left\{ \mathcal{R}_v (v_{\parallel} - v_{\parallel,o}) - (2 - 5s) v_{\parallel,o} \right\} \\ & + \left\{ \left(\mathcal{R}_v - \frac{2 - 5s}{\mathcal{H}_0 \chi} \right) \mathcal{H}_0 V_o + (\mathcal{R}_v + 1) \Psi - \mathcal{R}_v \Psi_o + (5s - 2) \Phi + \dot{\Phi} \mathcal{H}^{-1} + (b_e - 3) \mathcal{H} V \right\} \\ & + \left\{ \frac{2 - 5s}{\chi} \int_0^{\chi} (\Psi + \Phi) d\chi' + \mathcal{R}_v \int_0^{\chi} (\dot{\Psi} + \dot{\Phi}) d\chi' \right\} \end{aligned} \quad (2.1)$$

where

$$\mathcal{R}_v = 5s + \frac{2 - 5s}{\mathcal{H}\chi} + \frac{\dot{\mathcal{H}}}{\mathcal{H}^2} - b_e. \quad (2.2)$$

In Eq. 2.1, b_1 is the linear bias; s is the magnification bias; Ψ and Φ are the time-time and space-space parts of the perturbed gravitational potential; the subscript “ o ” indicates the peculiar velocity and potentials at the position of the Earth (observer); V is the velocity potential defined via $\vec{v} = -\vec{\nabla}V$; and overdots are partial time derivatives. \mathcal{R}_v follows the notation in [34], but a subscript v has been added for clarity to distinguish \mathcal{R}_v from the comoving curvature perturbation.

The terms in Eq. 2.1 are split the same way as [34]: Newtonian term (linear bias plus linear RSD); lensing; Doppler; local gravitational potentials; and integrated gravitational potentials. Each of these six terms appears respectively in the equation with six sets of brackets.

The biases b_1 , s , and b_e depend on the galaxy selection function. b_1 is the linear Eulerian galaxy clustering bias; s is the magnification bias, defined as the response of the galaxy

comoving number density, \bar{n} , to an infinitesimal change in the survey limiting magnitude m

$$s \equiv \frac{\partial \log_{10} \bar{n}}{\partial m}. \quad (2.3)$$

Recalling the conversion from magnitude to luminosity, this is identical to Equation 2.10 in [2]. Next, b_e is the evolution bias, the response of \bar{n} to an infinitesimal perturbation in redshift²

$$b_e = -(1+z) \frac{d \ln \bar{n}}{dz}. \quad (2.4)$$

As emphasized in [25], b_e and s are defined using partial derivatives that, respectively, hold the flux cut and the redshift constant. We follow this approach in our calculation of the Doppler bias in the next section, only varying the infinitesimal peculiar velocity and otherwise holding the selection criterion constant.

An important assumption of Eqs. 2.3 and 2.4 is that the response of the galaxy number density to redshifting and magnification is linear. This must be true for a sufficiently small change in magnitude or redshift, and has been explicitly tested for measurements of magnification bias in [23]. For the Doppler bias, we perform a similar test below, exploring the smallness of the stepsize. We furthermore note that the number density response should be linear on the characteristic scales of linear peculiar velocities, $v_{\text{rms}} \sim 150 \text{ km s}^{-1}$. If this is not satisfied, there could be higher-order corrections in Eq. 2.1, modifying the relationship between the Doppler bias and the observable galaxy power spectra.

The peculiar velocity biases described above (i.e. evolution bias and other terms in Eq. 2.2) break isotropy in the galaxy field, and lead to a nonzero dipole in the power spectrum and correlation function as their effects only impact the line of sight direction. Another major contributor to the dipole (and other odd multipoles) comes from wide-angle effects due to the galaxy power spectrum estimator definition with respect to the line of sight. Within the Yamamoto estimator for the galaxy power spectrum multipoles [35], the line-of-sight direction $\hat{\mathbf{d}}$ can be chosen separately for each galaxy pair with position vectors \mathbf{s}_1 and \mathbf{s}_2 :

$$\hat{P}_\ell(k) = \left\langle \frac{2\ell+1}{2A} \int d\mathbf{s}_1 \int d\mathbf{s}_2 \delta_g(\mathbf{s}_1) \delta_g(\mathbf{s}_2) e^{i\mathbf{k} \cdot (\mathbf{s}_1 - \mathbf{s}_2)} \mathcal{L}_\ell(\hat{\mathbf{k}} \cdot \hat{\mathbf{d}}) - S_\ell \right\rangle \quad (2.5)$$

where \mathcal{L}_ℓ is the Legendre polynomial of order ℓ , A is the normalization and S_ℓ is the shot noise. If the line-of-sight is chosen in a symmetry-breaking way, so that it is the same as the unit vector pointing to one of the galaxies, then the power spectrum can be calculated using fast Fourier transform methods which scale favorably with the large number of galaxy pairs in modern galaxy surveys [36–39]. This is referred to as the end-point line of sight definition in [29], in contrast to more symmetrical line-of-sight definitions that use the angular bisector or mean galaxy position vector.

However, breaking the symmetry between galaxies in a pair breaks parity symmetry and thus leads to a nonzero dipole [40]. The linear RSD term arising in the galaxy power spectrum assumes that the angle separating the galaxies is small. On large scales, this assumption breaks down [41–47], and the wide-angle contributions are especially large for the end-point line of sight choice [29, 46–48]. This contribution to the dipole and the octopole can be as large or larger than the contribution from peculiar velocities.

²Some authors define f_{evo} as our b_e plus 3; the extra factor of 3 accounts for the difference between comoving and physical number density. When using a comoving number density, $b_e = 0$ for dark matter, and when using a physical number density, so that $\rho \propto a^{-3}$, $b_e = 3$ [4].

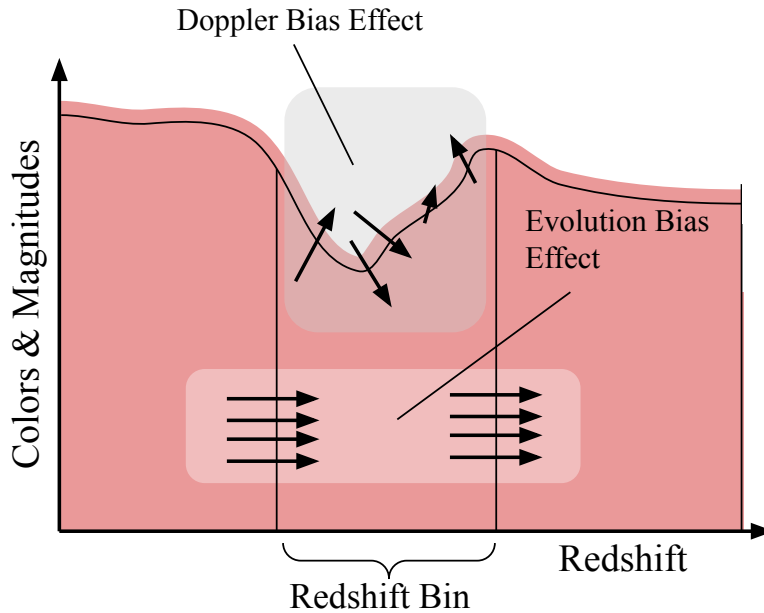


Figure 1: Schematic description of the Doppler bias computed in this paper, compared to the evolution bias defined in previous work. In this plot, the galaxies are selected below the wavy color cut and within the redshift bin. Evolution bias shifts galaxies left and right in this plot, affecting the redshift but not the color. However, redshifting also affects the fluxes, and therefore shifts the galaxies in the color direction as well. This effect is largest when emission lines are located at the boundary of each bandpass, where they pass in and out of the bands when shifted by the peculiar velocity. While the evolution bias only moves galaxies out of the selection if they are close to the redshift boundary, this is not necessarily the case for the Doppler bias. In practice, we compute the change in galaxy number, ΔN , from the evolution bias and the Doppler bias separately, and add them together.

Derivations of the magnification and evolution biases often assume a simple single-band flux or luminosity cut to define the galaxy sample. However, realistic galaxy samples, particularly in spectroscopic surveys, are much more complicated, with multiple flux and color cuts, often in different apertures (to eliminate failed redshifts of low surface-brightness galaxies or remove stars with point-source morphology). The impact of these subtleties on magnification bias is studied in [23]. Our paper extends similar considerations to the evolution bias.

2.2 Synthetic sample approach to measuring the Doppler bias

As with the magnification bias, the evolution bias must be defined for a specific multi-color galaxy selection, using the underlying galaxy spectra to determine the effects of peculiar velocity on the galaxy selection function. This means that evolution bias is more complex than the typical description of “derivative of the number density with respect to redshift.” Peculiar velocities affect galaxy fluxes as well as redshifts, by shifting emission features in and out of the bandpass used to define the flux. We therefore split the evolution bias into two parts: the previously-defined evolution bias b_e defined as the redshift derivative of the true comoving number density; and the impact of the Doppler shift on the observed fluxes,

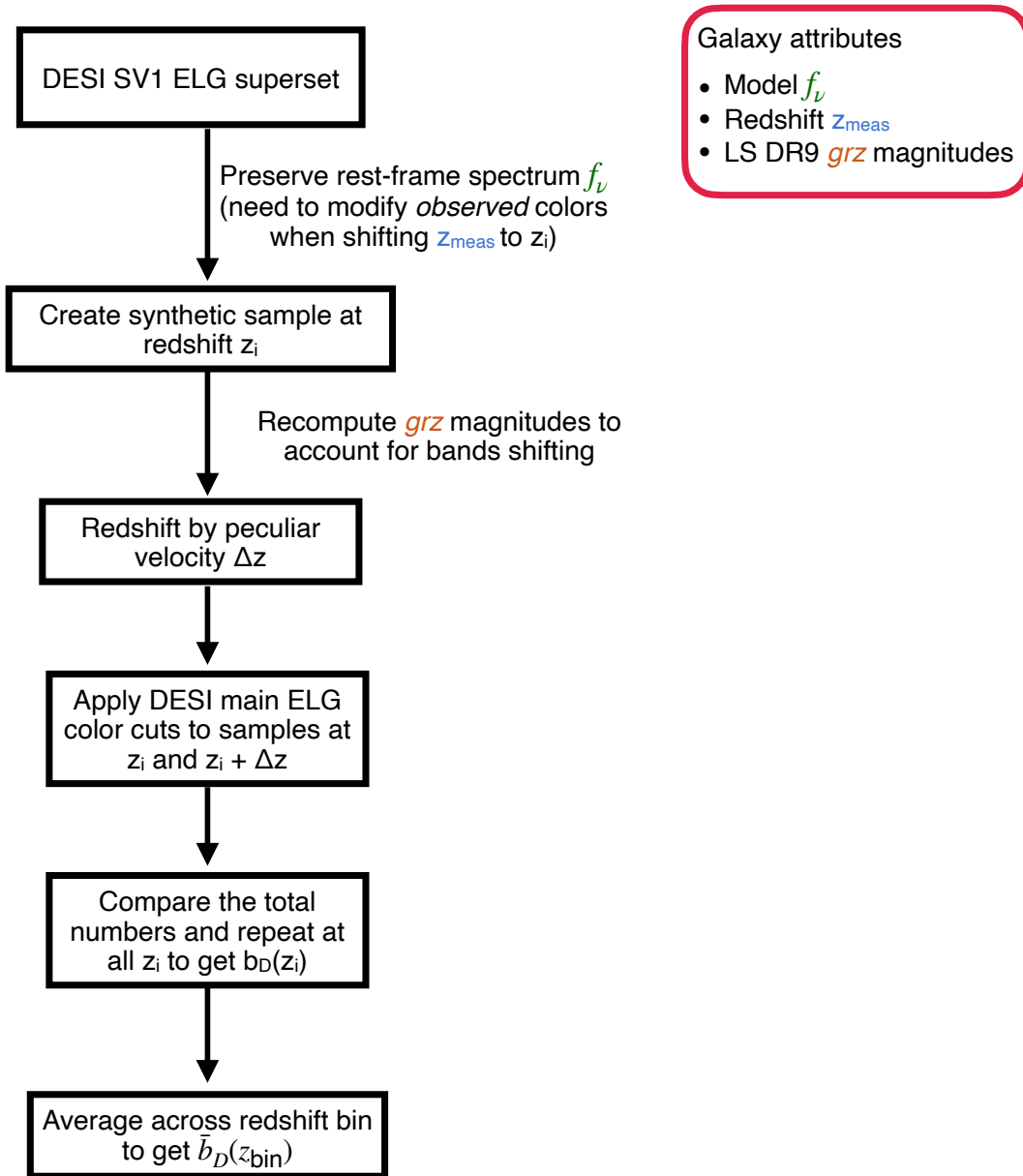


Figure 2: Flowchart summarizing our methodology. We start with the DESI SV1 ELG superset and use it to create synthetic samples at many closely spaced z_i , using real galaxies in the range $(z_i - 0.15, z_i)$ and preserving their rest-frame flux when shifting them to z_i . We then apply a small peculiar velocity to this sample, recompute its *grz* magnitudes, and compare the number of DESI main ELGs selected from the superset with and without the peculiar velocity. We then average within redshift bins to compute $\bar{b}_D(z_{\text{bin}})$, which can be directly related to LSS observables.

which we call the Doppler bias, b_D . Fig. 1 shows this schematically: evolution bias shifts the galaxy only right or left (changing the redshift) whereas Doppler bias can also shift the galaxies up and down (changing the fluxes). Unlike magnification bias, Doppler bias changes relative fluxes and thus colors, leading to additional effects from the color selection.

Similar effects have been considered previously, for instance in Refs. [25, 28]. Our work differs in a few respects. Ref. [25] considers the impact of K-corrections on the evolution bias for a single-band-selected galaxy survey, due to the fact that the peculiar velocity shifts a different part of the spectrum into the observed band. We go beyond this treatment in two respects: first, they calculate K-corrections assuming all galaxies have the same spectrum, and second, we consider a realistic galaxy color selection, which is far more complicated than a simple flux cut. Ref. [28] considers a very similar change in the CMASS galaxy selection induced by peculiar velocities; however, they directly estimate which galaxies are scatter into and out of the sample based on peculiar velocity reconstruction, rather than expressing the effect as an evolution-like bias like we do. Moreover, they consider the CMASS LRG sample, whereas we consider the DESI ELG sample which is much more susceptible to the Doppler bias.

Here we define the Doppler bias similarly to the evolution bias except N_{color} now refers to the number of galaxies within the color and magnitude selection cut:

$$b_D \equiv -(1+z) \frac{\ln N_{\text{color}}(z + \Delta z_{\text{pec}}) - \ln N_{\text{color}}(z)}{\Delta z_{\text{pec}}}. \quad (2.6)$$

Note that in this equation, we use the total number of galaxies within an observed redshift bin, $N_{\text{color}}(z)$, rather than the number density (number per comoving volume). The derivative is taken with respect to the line of sight peculiar velocity, $v_{\parallel} = \Delta z_{\text{pec}}/(1+z)$, rather than redshift. Therefore, in b_D , the redshift dependence of comoving volume does not contribute to the derivative, whereas in b_e , where we take a redshift derivative, it does contribute, and we must use the comoving number density \bar{n} .

In Fig. 2, we present a flowchart summarizing our methodology. We begin with a superset sample, described in Section 3, intended to contain all possible galaxies that could be part of the galaxy selection under consideration (the DESI ELG main survey selection). For each galaxy, we have a synthetic spectrum (the best-fit model spectrum as determined by the DESI redshift-fitting software), and integrate that spectrum to measure fluxes to determine how peculiar velocities change the galaxy colors. We then create synthetic samples at different redshifts (z_i), preserving the rest-frame flux for each galaxy, but moving galaxies to a common redshift to increase the sample size at each redshift and prevent confusion with redshift-dependent selection effects in the underlying superset. We then redshift all the galaxies under consideration by a small peculiar velocity Δz , compute the change in galaxy number density, and finally sum the change in number density over a specified bin in observed redshift to measure the Doppler bias b_D .

When including this term in our power spectrum calculations, we add b_D to all instances of b_e as they factor into the physics in the same way. Therefore \mathcal{R}_v in Eq. 2.2 becomes

$$\mathcal{R}_v = 5s + \frac{2-5s}{\mathcal{H}\chi} + \frac{\dot{\mathcal{H}}}{\mathcal{H}^2} - b_e - b_D. \quad (2.7)$$

ELG Biases	North	South
b_1	1.3	1.3
b_e	-1.2	-2.1
s	0.38	0.37
b_D	-2.7	-3.9
LRG Biases	North	South
b_2	2	2
b_e	8.1	10.2
s	1	1
b_D	0	0

Table 1: Biases used in the computations made with GaPSE for Emission Line Galaxies and Luminous Red Galaxies. These are averaged (weighted by number density) bias values over a redshift bin from 0.8 to 1.0. Note that different values were used for the North and South samples as each sample is slightly different.

2.3 Power Spectrum Dipole Calculation

The observables computed in this work were done using GaPSE,³ [5, 34, 49] a Galaxy Power Spectrum Estimator code written in Julia. More specifically, GaPSE computes all the full relativistic galaxy auto and cross correlation functions for an arbitrary multipole order, using the endpoint line of sight employed in the Yamamoto estimator. The correlation functions can be computed with or without an arbitrary window function. To speed up the evaluations, GaPSE takes advantage of an effective redshift approximation, which is shown to be accurate within $\sim 1\%$ (Fig. 4 of [5]) for narrow bins like the ones we considered.

We match the fiducial cosmology of the DESI collaboration [50], from the Planck 2018 TT,TE,EE+lowE+lensing marginalized means with a single massive neutrino of mass 0.06 eV [51]: $\Omega_b h^2 = 0.02237$, $\Omega_c h^2 = 0.1200$, $\ln 10^{10} A_s = 3.044$, $n_s = 0.9649$, $H_0 = 67.36 \text{ km s}^{-1} \text{ Mpc}^{-1}$.

3 DESI Emission Line Galaxy selection

We measure the Doppler and evolution biases using the DESI Emission Line Galaxy (ELG) sample released with the publicly available DESI Early Data Release (EDR) [52]⁴. DESI is a five-year survey targeting 40 million ELGs, Luminous Red Galaxies (LRGs), quasars, and low-redshift bright galaxies (BGS) at $0 < z < 2$ [53–55]. DESI measures 5000 redshifts at once using robotic fiber positioners across a 7.5 deg^2 field-of-view, with spectral resolution and wavelength coverage designed to measure redshifts from the [OII] doublet at $0.6 < z < 1.6$ [53, 56, 57]. The spectra are processed and reduced [58], and redshift fitting is performed automatically using the Redrock software [59].

The DESI EDR includes data taken for the Survey Validation (SV) phase [50] before the main five-year survey, in order to finalize targeting cuts, test observing strategy, and measure the linear galaxy bias for each sample. The first part of SV (SV1) was designed to finalize DESI targeting [60]: it uses looser target selection and longer integration times to achieve a high success rate on a superset of the final DESI targets. We use the superset defined by

³<https://github.com/foglieni/matteo/GaPSE.jl>

⁴<https://data.desi.lbl.gov/doc/releases/edr/>

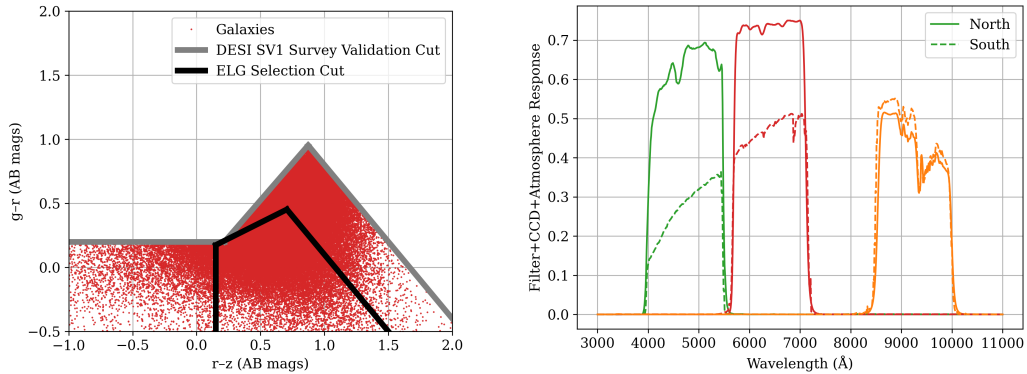


Figure 3: *Left:* distribution of DESI ELGs in grz space. More detail in Fig. 3 of [27]. The grey line shows the superset defined by early Survey Validation (SV1), whereas the black line shows the main survey ELG selection cut. We consider the SV1 ELGs as a superset within which galaxies can scatter into and out of the main survey ELG selection. Extinction correction has been applied to the galaxy magnitudes. *Right:* filter response curves for grz bands in the different imaging regions, BASS and MzLS (North; solid) and DECaLS (South; dashed). Filter curves include the entire system throughput (camera, atmosphere, telescope).

SV1 to measure the magnification, evolution, and Doppler biases for the main ELG selection. Measuring these biases requires a complete sample to take the derivative of the selection function with respect to redshift or luminosity.

We also use the One-Percent Survey of the third portion of SV (SV3) to measure galaxy clustering (and hence infer the linear bias) using data with very high fiber-assignment completeness. After DESI targets are selected, they must be assigned fibers [27]; due to the limited reach of each robotic fiber positioner, fiber-assigned targets cannot be closer than the 1.5 arcmin fiber patrol radius. This leads to distorted small-scale clustering as well as an incomplete sample, particularly for the ELGs, which have a target density of 2400 deg^{-2} and are expected to be only $\sim 80\%$ complete even after the five-year, five-pass main survey. A variety of methods have been proposed to eliminate the effects of fiber collisions from the main survey data [61–66]. In SV3, 20 separate fields are observed in a rosette pattern with 12–13 overlapping tiles (compared to the 5 overlaps in the DESI main survey), leading to $\sim 95\%$ fiber-assignment completeness for the ELG sample [52]. Using the SV3 data allows us to infer the linear bias directly from the clustering measurements without complicated corrections for incompleteness and fiber-assignment.

The DESI ELG sample is selected from the 3-band grz optical imaging of DESI Legacy Surveys Data Release 9 [67]. Data Release 9 consists of several observing programs: data north of declination 32.375° comes from the Beijing-Arizona Sky Survey (BASS) [68] for g and r -bands, and the Mayall z -band Legacy Survey (MzLS) for z -band. The rest of the imaging comes from DECam [69] on the 4-m Blanco telescope at CTIO, either using Dark Energy Survey (DES) data in its 5000 deg^2 footprint, or using the DECam Legacy Survey (DECaLS) where DES is not available [70]. When computing the impact of redshifting on the broad-band colors, we convolve the measured DESI spectra with the appropriate filter curves for BASS, MzLS, and DeCaLS,⁵ as shown in Fig. 3. Data reduction and photometry

⁵Available at <https://www.legacysurvey.org/dr9/description/>

is performed using the `legacypipe`⁶ and `Tractor` software [71], and photometry is measured using AB magnitudes. Each source is modelled with a point-source, exponential, de Vaucouleurs or Sèrsic profile, and both total fluxes and fiber fluxes (flux within a 1.5 arcsec DESI fiber convolved with 1 arcsec Gaussian seeing) are reported [27]. The depth varies between footprints: in the North, the 5σ g -band depth is $g = 24.1$,⁷ just above the limiting magnitude of ELG selection of $g_{\text{fib}} = 24.1$, whereas the depth is $g = 24.5$ in the South-DECaLS region and $g = 24.9$ in the South-DES region. Here the subscript “fib” refers to the g magnitude measured within a 1” DESI fiber, as opposed to the total magnitude, which is given without a subscript. We always use extinction-corrected photometry, following DESI target selection and using the extinction map of [72]. While the impact of updated extinction corrections on the ELG target selection may be substantial [73], we choose to continue to use the SFD extinction map for consistency with the original DESI target selection.

DESI ELGs are selected using a simple color cut on $g - r$ and $r - z$ colors, and a cut on g_{fib} . We study the `ELG_LOP` selection, as shown in Table 2 of [27], which is designed to target ELGs at $1.1 < z < 1.6$, though in practice selects ELGs over a broader redshift range, $0.6 < z < 1.6$. The ELG selection that we use is given by the following color cuts:

$$\begin{aligned}
 r - z &> 0.15 \\
 g - r &< 0.5 \times (r - z) + 0.1 \\
 g - r &< -1.2 \times (r - z) + 1.3 \\
 g &> 20 \\
 g_{\text{fib}} &< 24.1
 \end{aligned}
 \tag{3.1}$$

The SV1 selection extends the color selection in all directions, as shown in Figure 4 of [27] and listed in Table A.1 of [27]. The color cuts are the same in the North and South imaging regions, even though the photometric systems are slightly different. For clarity, we reproduce the distribution of the DESI ELGs in grz color space in Fig. 3, and also show the SV1 superset and the main survey ELG selections.

We start by selecting all 181,144 SV1 ELGs. We then remove ELGs with unreliable spectroscopic redshifts, as measured by a simple cut using the [OII] flux signal-to-noise `FOII_SNR` and the $\Delta\chi^2$ between the best-fit redshift and the second-best fit [27]:

$$\log_{10}(\text{FOII_SNR}) + 0.2 \log_{10}(\text{DELTA_CHI2}) > 0.9
 \tag{3.2}$$

This leaves 103,249 ELGs. We also remove any spectra classified as quasars by the quasar afterburner pipeline [74], leaving 98,318 ELGs. This number is similar to (but slightly different) from the number of SV1 ELGs reported in Table 6 of [52], due to the different criterion used for a good redshift. 40,098 ELGs are located in the North, and 58,220 are in the South. `Redrock` returns both the measured spectrum and a best-fit model spectrum; we use the best-fit model spectrum to compute synthetic magnitudes and thus the Doppler bias. We additionally remove 814 galaxies where the model fluxes are negative or missing. 99 of these galaxies are actually stars and the galaxy template for stars is missing. The other 715 are cases where the template flux is negative, which is allowed by `Redrock` to model low signal-to-noise spectra; in some of these cases, the observed spectra can be negative due to sky-subtraction issues. We tested recovering these 715 galaxies by adding a constant offset to enforce that the template

⁶<https://github.com/legacysurvey/legacypipe>

⁷Measured for a 0.45 arcsec exponential profile, as reported in Table 1 of [27].

is always positive. Since we only care about the difference between the non-redshifted and peculiar-velocity redshifted magnitudes, the constant offset should make a minimal impact on the difference. We find no difference in Fig. 4 when we make this change. Since it is an ad hoc correction, by default we remove these 715 galaxies from our sample.

4 Measuring the Doppler bias

Our process for measuring the Doppler bias involves a number of steps, and is summarized in the flowchart in Fig. 2. The basic philosophy is to construct a synthetic sample of ELGs at each redshift (z_i) across a finely spaced grid between $z_0 = 0.6$ and $z_n = 1.6$, with sufficient sample size to accurately measure the Doppler bias, and then apply the DESI ELG selection cuts to the synthetic sample.

4.1 Creating the synthetic sample at each redshift

Our ELG synthetic samples consist of galaxies shifted to a grid of redshift values z_i . On this grid, the bins of galaxies that are shifted to these z_i overlap significantly such that nearby galaxies are in some sense copied to nearby redshift locations to cover our overall redshift range from $z = 0.6$ to $z = 1.6$ more completely. When constructing our ELG synthetic samples, we start by redshifting all galaxies within a particular redshift range to z_i . We refer to the original redshift of each galaxy as $z^{\text{meas},j}$ and each redshift under consideration on the finely spaced grid as z_i .⁸ The superscript j refers to the galaxy under consideration, while i refers to the particular redshift in our well populated superset.

We shift to z_i for two major reasons. First, we want to measure the Doppler bias in very narrow bins of redshift z_i , since the [OII] emission line is narrow and the impact of redshifting it may change rapidly across a small change in redshift. However, this would lead to very narrow bins of ELGs, with very few galaxies in each bin, making it difficult to measure the Doppler shift well. Second, if we simply used each galaxy at its measured redshift, this could imprint the redshift selection function into our estimation, which is very undesirable. It may be that the SV1 superset observes galaxies less efficiently at certain redshifts (e.g. due to variations in the DESI instrument or atmospheric lines[75]), and could have peculiar velocity selection effects already imprinted on it. We therefore wish to avoid this situation, by creating a synthetic sample of galaxies at the (assumed to be) true redshift under consideration, constructed from as many of the SV1 ELGs as feasible.

Specifically, for a bin at redshift z_i , we select all galaxies between $z_i - 0.15$ and z_i and redshift their model spectra to z_i , and then compute the Doppler bias as if all of those galaxies were at z_i . The width of the bin, 0.15, is chosen to balance considerations of ensuring a sufficiently large sample size, against potential redshift evolution in the ELG samples. We test that our results are very similar if we change the width to 0.1 or to 0.2.

We only consider galaxies at redshifts less than z_i (rather than a symmetric range between $z_i - 0.15/2$ and $z_i + 0.15/2$) because we find that the model spectra can suffer from issues when extrapolated outside of the DESI wavelength coverage of 3600 Å to 9800 Å. In particular, when the model spectra are not constrained by data, there is nothing preventing them from dropping below zero. This becomes an issue when shifting the galaxies to lower redshifts, since the upper wavelength coverage of DESI (9800 Å) is slightly less than the upper

⁸We neglect redshift uncertainties in this procedure; this is self-consistent because we always use the synthetic spectrum to determine magnitudes. The only redshift error which could affect this procedure is a catastrophic redshift error, which are $< 0.2\%$ of the sample [27].

wavelength of the z -band (10000 Å). On the other hand, DESI’s lower wavelength of 3600 Å is quite a bit shorter than the blue end of the g -band (4000 Å). The upper cutoff would thus lie within the z -band for galaxies with redshift greater than z_i (causing issues with spurious negative flux); but the lower cutoff does not move into the g -band for galaxies with redshift greater than $z_i - 0.15$. Hence, due to this asymmetry between the DESI spectrum coverage and the bandpass locations, we only consider galaxies at $z^{\text{meas},j} < z_i$ when constructing the superset at each z_i .

4.2 Measuring synthetic magnitudes and redshifting them

To compute synthetic grz magnitudes for each galaxy, we start with the model DESI spectra, which are given at $z = 0$, redshift them to $z^{\text{meas},j}$, and convolve with the appropriate filter response curve [76]. This begins with the filter response convolution operator.

$$F[S_a, f_\lambda] = \int_0^\infty d\lambda f_\lambda(\lambda/(1 + z^{\text{meas},j})) S_a(\lambda) \frac{\lambda}{hc}, \quad (4.1)$$

where h is Planck’s constant and for clarity, we have not set c to 1. Additionally, $f_\lambda(\lambda)$ is the rest-frame model DESI spectrum for each object, corrected as described below, $S_a(\lambda)$ is the filter response curve as shown in Fig. 3, and a indexes the filters grz .

To compute the magnitudes, we normalize with the model AB reference source which is used to define the photometric system’s zeropoint: $F[S_a, f_{\lambda,0}]$. The reference flux density for the AB system is defined:

$$f_{\lambda,0}^{AB}(\lambda) = \frac{c}{\lambda^2} (3.631 \times 10^{-20} \text{erg s}^{-1} \text{cm}^{-2} \text{Hz}^{-1}). \quad (4.2)$$

Normalizing the filter response convolution operator and simplifying, we obtain

$$\frac{F[S_a, f_\lambda]}{F[S_a, f_{\lambda,0}]} = \frac{\int d\lambda f_\lambda(\lambda/(1 + z^{\text{meas},j})) S_a(\lambda) \lambda}{(3.631 \times 10^{-20} \text{erg s}^{-1} \text{cm}^{-2} \text{Hz}^{-1}) \int d\lambda S_a(\lambda) c/\lambda}. \quad (4.3)$$

We then convert flux to AB magnitude

$$m_a = -2.5 \log_{10} \left(\frac{F[S_a, f_\lambda]}{F[S_a, f_{\lambda,0}]} \right) = -2.5 \log_{10}(\langle f_\nu \rangle_a) - 48.6, \quad (4.4)$$

where

$$\langle f_\nu \rangle_a = \frac{\int d\lambda f_\lambda(\lambda/(1 + z^{\text{meas},j})) S_a(\lambda) \lambda}{\int d\lambda S_a(\lambda) c/\lambda}. \quad (4.5)$$

We apply a small correction to the model DESI spectra to remove unphysical negative emission lines. These arise because **Redrock** does not place any physical priors on the emission and absorption lines. One particularly common failure mode in the ELG spectra is [OIII] 4959 and 5007 Å absorption rather than emission, likely tied to sky subtraction residuals from OH skylines at the red end of the spectrum. This can create strongly negative flux in the [OIII] region, leading to a negative overall flux or spurious flux shifts related to the redshifting of these unphysical absorption lines. We correct models with unphysical absorption by fitting a line to the emission spectrum values in the ranges of 4910(1 + z) to 4935(1 + z) Å and 5060(1 + z) to 5084(1 + z) Å on either side of the lines. Then we replace the points in the spectrum with the linear fit in these ranges if the points are more than two standard deviations below the linear fit.

After computing m_a , we have two measurements for the broad-band photometry for each galaxy: the synthetic magnitudes from Eq. 4.3, and the broad-band fluxes from the Legacy Survey DR9 imaging survey. In theory, these two measurements should be exactly consistent with each other;⁹ however, in practice, due to observational errors (i.e. Poisson noise on the measured fluxes and spectra), this is not the case. Since the DESI target selection uses the broad-band fluxes from the imaging, we start with the DR9 fluxes, and only use the synthetic magnitudes to measure the *shifts* in magnitude due to peculiar velocity. That is, for each galaxy indexed by j , when applying a peculiar velocity of Δz , we compute

$$\mathcal{S}_{a,z \text{ only}}^j(z, z + \Delta z) = m_a^j(z + \Delta z) - m_a^j(z) \quad (4.6)$$

using the synthetic magnitudes from Eq. 4.4; or equivalently, writing the shift function \mathcal{S} in terms of fluxes

$$\mathcal{S}_{a,z \text{ only}}^j := f_\lambda(\lambda/(1+z)) \rightarrow f_\lambda(\lambda/(1+z+\Delta z)) \quad (4.7)$$

where $\mathcal{S}_{a,z \text{ only}}^j$ is the function that modifies the magnitudes of the j th galaxy corresponding to a redshift from z to $z + \Delta z$. The notation above is defining \mathcal{S} as the operation that shifts $f_\lambda(\lambda/(1+z))$ by Δz , the operation indicated with the arrow. When applying the small redshift of Δz , we do *not* also modify the flux to account for the increased luminosity distance, since changes in galaxy brightness are treated separately in Eq. 2.1 and are related to the magnification bias s . We indicate this with the subscript “z only.”

We also modify the observed fluxes to preserve the rest-frame f_ν , when shifting from $z^{\text{meas},j}$ to z_i . Since we are setting up the ELG superset, in this step we *do* scale the observed flux with the luminosity distance

$$\mathcal{S}_{z + D_L \text{ shift}}^j := f_\lambda(\lambda/(1+z^{\text{meas},j})) \rightarrow f_\lambda(\lambda/(1+z_i)) \frac{D_L(z^{\text{meas},j})^2}{D_L(z_i)^2} \frac{1+z^{\text{meas},j}}{1+z_i} \quad (4.8)$$

As described above, we consider an asymmetric set of galaxies, redshifting those within $(z_i - 0.15, z_i)$ to z_i . As a result, the galaxies are always fainter when moved to z_i , since they are all moved further away. The effect of the Doppler bias on galaxy selection depends both on the impact of the peculiar velocity on the spectrum, and the underlying distribution of galaxies as a function of their rest-frame spectrum. In particular, it cares about the distribution of galaxies close to the flux cuts, and if the galaxies are all made fainter, we will be probing a different set of galaxies than we otherwise would have. This would cause the synthetic sample to measure a different, incorrect, Doppler bias from the true Doppler bias of the underlying ELG sample. To correct for this, we *brighten* all galaxies by an amount corresponding to a shift of 0.075 in redshift, i.e. half of the redshift bin used to construct the superset. Therefore, the final shifted magnitudes for each galaxy are given by:

$$m_a^{\text{shifted},j} = m_a^{\text{LS,meas},j} + \mathcal{S}_{z + D_L \text{ shift} - D_L(\Delta z = 0.075) \text{ shift}}^j(z^{\text{meas},j}, z_i) + \mathcal{S}_{z \text{ only}}^j(z_i, z_i + \Delta z) \quad (4.9)$$

where the subscript “ $-D_L(\Delta z = 0.075)$ shift” indicates the brightening described in the previous paragraph. We compute the number of galaxies passing the ELG selection cut for the shifted magnitudes, and also for unshifted magnitudes

$$m_a^{\text{unshifted},j} = m_a^{\text{LS,meas},j} + \mathcal{S}_{z + D_L \text{ shift} - D_L(\Delta z = 0.075) \text{ shift}}^j(z^{\text{meas},j}, z_i) \quad (4.10)$$

⁹The synthetic magnitude should agree exactly with the fiber magnitude, since the fiber magnitude is measured within an aperture that is the same size as a DESI fiber; the total magnitude will be different since it captures more light.

An important assumption in this approach is that the superset is sufficiently complete, i.e. that it contains all galaxies that could have scattered into the underlying ELG selection due to peculiar velocities. This means that the superset must have a buffer around the DESI ELG selection, with width equal to the typical shifts in $g - r$ and $r - z$ colors. The typical shifts in these colors are very small, ~ 0.005 mags, with the largest shifts reaching up to ~ 0.2 mags. As shown in Fig. 3, the SV1 ELG cuts are nearly always sufficiently far away, except in the region around $r - z \sim 0.15$, $g - r \sim 0.3$, where the two selections cross. This region in color space is mostly populated by higher-redshift ELGs (Fig. 4 in [27]), and is sparsely populated at $z < 1.2$. We test for the effects of incompleteness by shifting the second color cut in Eq. 3.1 by 0.05 magnitudes, since b_D at $0.8 < z < 1$ is determined by galaxies shifting across this color cut. As we discuss in Section 4.4 below, we find that b_D is somewhat sensitive to incompleteness.

4.3 Measuring the change in number of ELGs

After the magnitudes are shifted, we count the number of galaxies within the DESI ELG selection cut before and after the peculiar velocity shift. We conduct a convergence test along similar lines as that described in [23]. We start by computing two-sided derivatives, i.e. measuring

$$\Delta N(\Delta z_{\text{pec}}) = N_{\text{color}}(z + \Delta z_{\text{pec}}) - N_{\text{color}}(z - \Delta z_{\text{pec}}) \quad (4.11)$$

$$b_D = -(1 + z) \frac{\Delta N(\Delta z_{\text{pec}})}{2\Delta z_{\text{pec}} N_{\text{color}}(z)} \quad (4.12)$$

Determining b_D in this way has errors that are quadratic in the step-size Δz [23, 77]. Thus, we measure ΔN for several different step sizes. We then create independent samples by differencing ΔN between sequentially larger step sizes, measuring \hat{b}_D in each step, and fitting a quadratic as a function of increasing step size. If Δz_{pec} is small compared to the scales on which b_D varies, the quadratic will be a good fit, and evaluating the quadratic at a stepsize of zero will be the optimal estimator for b_D . We can perform this test at each redshift, z_i under consideration on our grid. We test values of z_{pec} ranging between 0.001 and 0.005 (i.e. stepsizes between 0.002 and 0.01). We find that at some z_i , the quadratic is a good fit, but at others, it is not.¹⁰ This points to sharp changes in b_D as a function of the step-size, which is not surprising given the sharpness of the spectral features under consideration (most prominently [OII] emission, but also other features as well). This means that the fit should contain higher even powers of Δz , which can have large coefficients making them larger than the Δz^2 term. We could push to even smaller values of Δz_{pec} ; however, the resolution of the filter bandpasses, $S_a(\lambda)$, corresponds to $\Delta z_{\text{pec}} \sim 0.027$ for [OII] redshifted to $z = 1$, and thus a smaller Δz_{pec} will unavoidably miss even finer features in b_D that come from features in the filter curves that are simply not measured at the resolution that is available. Balancing these considerations, the best procedure is to use a two-sided derivative with $\Delta z_{\text{pec}} = 0.001$, which is the smallest step-size resolvable given the filter resolution, and avoids extrapolating to smaller step-sizes assuming the validity of the quadratic fit. The plot illustrating this test is shown on the right hand side of Fig. 4, and shows that different choices for the step-size make very little difference.

¹⁰A further subtlety arises from the likelihood that is minimized when the quadratic is fit. In the low- N limit, it becomes important to consider that we are differencing two Poisson distributions. Thus, the likelihood is not necessarily Gaussian. We find that some of the bad fits are in the low N limit, but some of them are also at very large N where the central limit theorem guarantees Gaussianity, implying that the poor fits are due to intrinsic variability in b_D as a function of stepsize, not non-Gaussianity of the fitted likelihood.

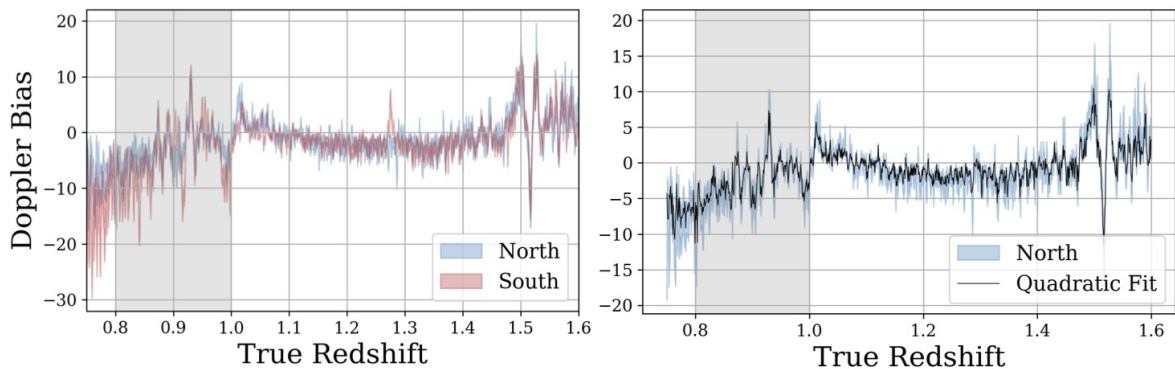


Figure 4: *Left:* Doppler bias for the North and South samples, with the 1σ uncertainty band given by the shaded region. We emphasize that the Doppler bias is computed as a function of the redshift, z_i , of the ELGs, and to determine its impact on observables, it must be averaged across a bin in observed redshift. The grey rectangle shows the 0.8–1.0 redshift range that we study further since it has the largest b_D impact. *Right:* Comparison between two methods for estimating the Doppler bias: the smallest step size considered of $\Delta z = 0.002$ (solid; fiducial method), and a quadratic fit to Doppler bias measured in step sizes between $\Delta z = 0.002$ and 0.01 (dashed), to ensure that the results are independent of step size. The two results are nearly indistinguishable.

4.4 Doppler bias measurement

We show the estimated b_D in Fig. 4 between the North and the South. On the right panel, we compare the results from the quadratic fit to those from the smallest step-size considered of $\Delta z_{\text{pec}} = 0.001$. The results are nearly indistinguishable; as a result, our results are robust to convergence issues caused by a too-large Δz_{pec} .

It is important to note that Fig. 4 is not an observable quantity, but rather gives the Doppler bias as a function of redshift z_i in our constructed ELG supersets. Determining the impact on observables (i.e. galaxy power spectra) requires averaging b_D within some pre-defined bin in *observed* redshift.

The Doppler bias shows many narrow features, corresponding to specific redshifts where strong emission lines redshift into and out of the bandpasses. The b_D features are slightly more prominent in the South filters, mostly due to the sharper drop at the red end of the South r -band, and the notch in the South r -band at 6900 \AA (Fig. 3).

In Figure 5, we explore some specific redshifts and plot some example spectra to explain where the trends in Fig. 4 are coming from. This figure shows the origin of some of the most prominent features in Fig. 4. There are several features at $z < 1$ coming from [OII] shifting across features in the r -band filter that decrease the r magnitude. Peculiar velocity shifted galaxies are thus fainter in the r -band, which makes $g - r$ smaller and $r - z$ larger, thus shifting galaxies down and to the right in the color-color plot. This causes many galaxies to scatter into the ELG color selection, resulting in a positive derivative of N_{color} and thus a negative Doppler bias. These features are prominent at $z = 0.8410$ ([OII] passing over the notch in the South r -band at 6900 \AA); $z = 0.9159$ from [OII] passing out of the r -band at 7100 \AA ; and a rise at $z = 0.9303$ and a dip at $z = 0.9386$ from [OII] passing over a small rise and dip in r -band at 7200 \AA just after the steep dropoff of the r -band at 7100 \AA .

There are also a number of features arising from emission lines passing into and out of

the z -band. The beginning of z -band at 8500 \AA is more gradual than the end of r -band at 7100 \AA ; hence the b_D rise at $z = 1.276$ is less prominent than the dip at $z = 0.9159$, and only present in the South where the z -band filter rises more steeply. The most prominent features caused by z -band are the rises and dips at $z = 1.4979, 1.5158, \text{ and } 1.5260$. These come from [OII] passing over some large features in the middle of the z -band filter, starting around 9350 \AA ; these features are present in both the North and South z -band filters and are thus present in both the North and South b_D curves. Other features come from the [OIII] emission lines at $4959 \text{ and } 5007 \text{ \AA}$. The dips at $z \sim 0.99$ come from these lines passing out of the z -band at 10000 \AA . The dips at $z = 0.8605 \text{ and } 0.8820$ come from the more prominent of these lines, [OIII] 5007 \AA , passing over the dips in the middle of z -band at $9350 \text{ and } 9450 \text{ \AA}$.

In addition to the narrow features created by the lines, there is also a broad trend for slightly negative b_D at $z < 1$, and nearly zero b_D at $z > 1$. This is likely coming from the broad Balmer break at $3700\text{--}4000 \text{ \AA}$ passing out of the r -band, creating a similar negative b_D feature to the one created by [OII] passing out of the r -band, but extended over a much larger region because the Balmer rise is much more gradual than the [OII] line. We single out the redshift range 0.8 to 1.0 , which includes several of the largest narrow spikes, as well as the broad-band feature of negative b_D coming from the Balmer break. Since this is the redshift range where b_D is largest, we study its impact on clustering statistics in this range by considering the clustering of a bin of ELGs at these redshifts. As emphasized in Fig. 2 above, this requires us to translate from b_D as a function of redshift, z_i , to an observable quantity that gives the impact of the Doppler bias in the clustering in a particular redshift bin. To average b_D within the bin, we compute the corresponding $\Delta N/N$ at each z_i , multiply by the comoving number density $\bar{n}(z_i)$, sum ΔN , and then finally divide by the summed comoving number density. We find an averaged b_D of -3.9 for the South sample and -2.7 for the North. We then use this value as input to GaPSE in Section 6. There are larger features in b_D around $z \sim 1.5$ than around $z \sim 0.9$. However, since they are both positive and negative, when averaging in a bin from $1.4 < z < 1.6$, we find that b_D is $\sim 3\times$ smaller than at $0.8 < z < 1.0$. Furthermore, we lack another high-density tracer at $1.4 < z < 1.6$, unlike at $0.8 < z < 1$ where the LRGs are convenient for cross-correlation. As a result, we focus on $0.8 < z < 1$ where the effects of b_D are largest and most easily detectable. As discussed in Sec. 4.2, our results could be affected by incompleteness in the parent ELG sample at $r - z \sim 0.15, g - r \sim 0.3$. The density of $z \sim 0.9$ galaxies is relatively low in this region in color-space (where the average redshift is typically higher), so incompleteness should only have a modest impact on b_D at these redshifts. However, if we are missing galaxies from the superset, this would cause us to under-estimate b_D at $z \sim 0.9$, where peculiar velocities are causing galaxies to enter the ELG sample by making them fainter in g magnitude. If the superset is incomplete, then even more galaxies should scatter into the sample than we observe, leading to a larger, even more negative b_D . We find that our results are rather sensitive to the selection cut in $g - r$ and $r - z$, with a 0.05 change in magnitude leading to $\Delta b_D \sim 3$ (although the broad trends and positions of the narrow spikes are qualitatively similar). This suggests that our results are sensitive to incompleteness in the parent sample. Future work with more extended parent samples may therefore be necessary to more accurately measure b_D .

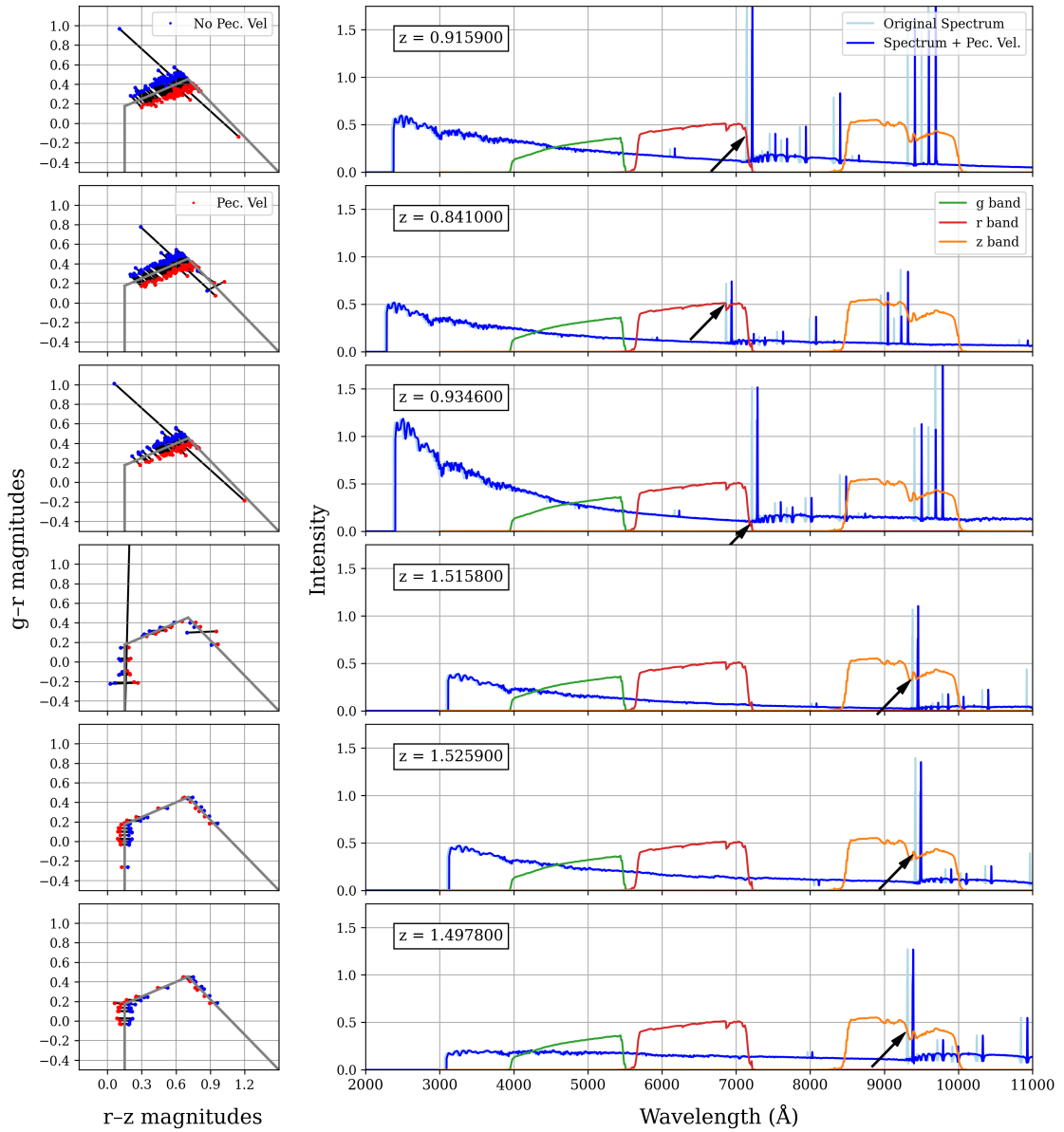


Figure 5: *Left:* ELG $g - r$ and $r - z$ color shifts. Each point shows an ELG at redshift z_i , comparing measured (blue) and velocity-shifted (red) photometry. Only ELGs that cross the DESI ELG selection box (grey) when shifted with small peculiar velocity are shown. Shifts are scaled by a factor of 10 for clarity. *Right:* Example spectrum at z_i with South grz filters, comparing original (light blue) and velocity-shifted (dark blue) spectra, shifted by an exaggerated $z = 0.02$ for visibility. Arrows highlight where the [OII] line aligns with a sharp filter drop, causing magnitude shifts in the color-color plots.

Redshift	b_1
0.85	1.25 ± 0.08
0.95	1.17 ± 0.07
1.05	1.29 ± 0.09
1.15	1.23 ± 0.08
1.25	1.30 ± 0.09
1.35	1.59 ± 0.10
1.45	1.72 ± 0.10
1.55	1.41 ± 0.14

Table 2: Linear bias for the ELG sample, measured from the projected correlation function at $20 < r_p < 80 h^{-1}$ Mpc.

5 Linear bias, magnification bias and evolution bias

5.1 Linear bias

We estimate the linear bias b_1 from the projected correlation function w_p of the SV3 ELGs at $20 < r_p < 80 h^{-1}$ Mpc, comparing the measured w_p to the expectation from the HALOFIT nonlinear power spectrum [78] as computed by CAMB in the fiducial cosmology [79, 80]. As we see in Table 2, the linear bias is approximately constant until $z = 1.3$, and increases thereafter.

Since the peculiar velocity terms are enhanced in the multi-tracer dipole proportional to the difference in linear biases, we explored the prospect for splitting the ELG sample into multiple subsets. We measured ELG clustering in bins split by g magnitude, but found that the linear bias of the different ELG bins was very similar. Other splits in ELG properties may yield a larger bias difference [e.g. 81], but we do not consider them here. Instead, we considered the cross-correlation between ELGs and LRGs, which overlap the ELGs well, especially at $z \sim 0.9$ where the Doppler bias is largest, and give us a large sample of galaxies with considerably higher linear bias.

The LRG sample has been well-characterized in past work (e.g. tomographic CMB lensing cross-correlation) and we therefore use $b = 2$ and $s = 1$ [82, 83]. We compute the evolution bias from the measured number density $\bar{n}(z)$ in the same way as for the ELGs. LRG target selection uses the infrared WISE W1 and W2 bands (3.4 and 4.6 μm) in addition to grz . We do not have model spectra at these wavelengths, so we cannot calculate the Doppler bias for the LRGs. However, since the LRGs are dominated by continuum emission rather than emission lines, we expect the Doppler bias to be negligible, and therefore set it equal to zero in the power spectrum calculation.

5.2 Magnification bias

The magnification bias is sensitive to the overall distribution of g_{fib} and g magnitudes, since lensing magnification is achromatic and leaves the $g-r$ and $r-z$ colors unchanged. As shown in Eq. 3.1, there is no ELG selection cut that couples together colors and magnitudes; hence, the only changes that will matter for magnification are those that affect the upper and lower flux limits, $g > 20$ and $g_{\text{fib}} < 24.1$.

As a result, we use a slightly different (and simpler) procedure to measure magnification bias than the synthetic sample approach described in Section 4. Redshifting galaxies from

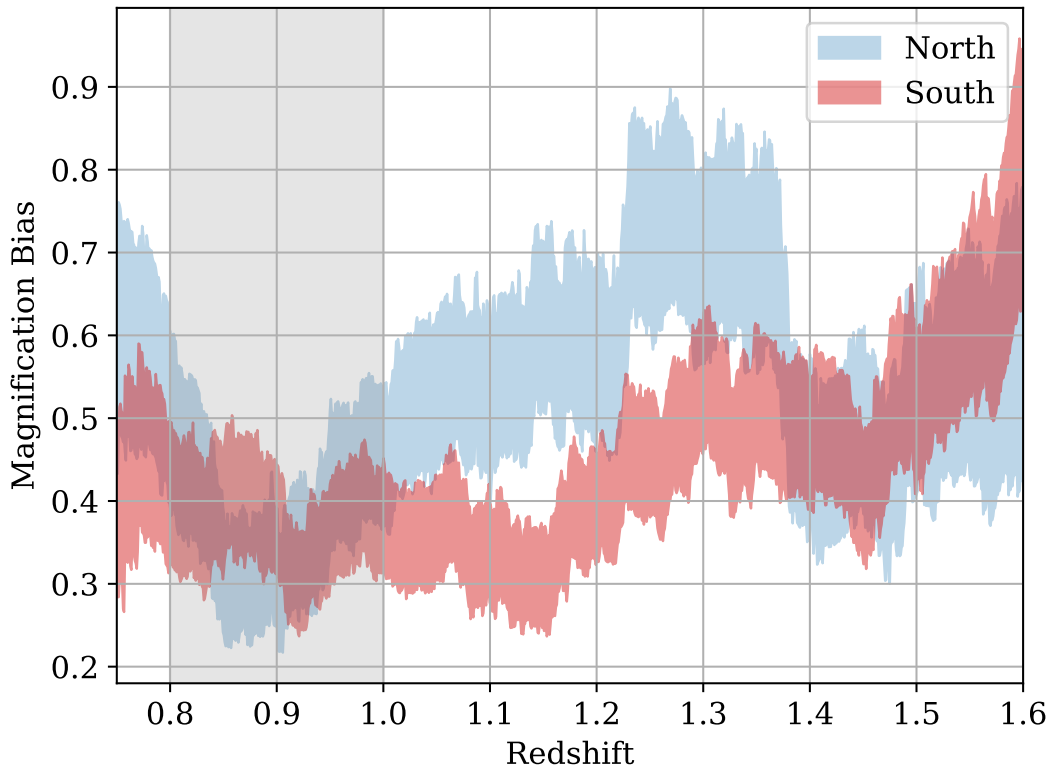


Figure 6: Magnification bias for North and South galaxy samples, showing the 1σ uncertainty band (shaded). The grey rectangle shows the 0.8–1.0 redshift range that we study further since it has the largest b_D impact.

$z^{\text{meas},j}$ to z_i (including the flux scalings to preserve the rest-frame f_ν) modifies the g and g_{fib} distributions away from the observed distributions, which can substantially change the magnification bias.¹¹ This is largely due to the diversity in spectral shapes of the ELGs, which adds scatter to the redshifted magnitudes and thus broadens the distributions of g and g_{fib} . The SV1 sample extends to slightly deeper g_{fib} than the main ELG selection, but not so much deeper that all galaxies that could scatter into the main ELG selection from redshifting are included. As a result, the g and g_{fib} distributions for the synthetic sample ELGs are somewhat distorted relative to the true distribution, due to the imprint of the underlying SV1 ELG selection function. The measured g and g_{fib} distributions (at a specific redshift or within a given range of redshifts) are thus a better approximation of the true distribution.

To measure the magnification bias at z_i , we therefore use the measured magnitudes of all galaxies within a bin between $z_i - 0.075$ and $z_i + 0.075$, matching the size of the bins used in the synthetic sample approach—as before, the bin at each redshift is expanded to increase the sample size and improve the precision with which we can measure the magnification bias. We do *not* modify the magnitudes by redshifting the galaxies to z_i .

¹¹Note that the change in g and g_{fib} distributions does not affect the Doppler bias much, which is largely determined by the color changes, as shown in Fig. 10.

After creating the sample, measuring magnification bias is straightforward. Since we have the parent sample of galaxies, we can simply magnify the sample by a certain amount and measure the change in number, unlike the two-direction shifting described in [23, 24] to measure magnification bias in the case where only the final targeted sample is available. We therefore add $\Delta m = 0.01$ to each magnitude, and compute the magnification bias by taking the finite difference of the number of galaxies at the shifted magnitude, and the original number of galaxies.

We only shift the galaxy magnitudes fainter (increasing the magnitudes) because the faint end of the ELG sample is close to the detection limit in the North imaging ($g = 24.1$ at the 5σ limit for a 0.45 arcsec exponential profile in g -band, from Table 1 in [27]). Shifting the magnitudes brighter (decreasing the magnitudes) would mean that magnification would add galaxies to the sample that were not detected in the original Legacy Survey imaging. Since these galaxies are by definition not in the catalog, our measurement of magnification bias would therefore be biased.

A magnification by 0.01 magnitudes does not increase fiber magnitudes by the same amount for all types of galaxies. Since lensing magnification makes galaxies bigger but preserves surface brightness, fixed-aperture magnitudes cannot receive the entire increase in flux, since part of the magnified galaxy is moved outside the aperture. Following [83], we assume that the total fluxes receive all of the change in flux from magnification, but the impact on fiber magnitudes is reduced. Following Appendix C in [83], we translate the change in total magnitudes to the change in fiber magnitudes. Of the faintest 0.01 magnitudes of main selection ELGs, we find that 29.6% are point sources, 59.6% are round exponential, 8.8% are exponential, 2.0% are deVaucouleurs and 0% are Sersic. We interpolate the fiber flux divided by the total flux as a function of half-light radius (or half-light radius and aspect ratio for de Vaucouleurs galaxies), and then weight by the observed distribution of half-light radius and aspect ratio. Weighting by the distribution of each type, we find a response of 0.8 (i.e. magnification of the flux by a factor F increases the fiber flux by $0.8F$), which is constant with redshift. The response is larger than that found by [83] for DESI LRGs, because the faint end ELGs are fainter and more point-source-like.

We show the magnification bias as a function of the redshift in Fig. 6. Averaging between 0.8 and 1.0 (again weighting by the comoving number density), we find $s = 0.36$ for North and $s = 0.37$ for South. Our values for magnification bias are lower than those of [84], who find $s = 0.89$, also for DESI ELGs. However, they are using the ELG target sample combining both ELG_LOP and ELG_VLO selections, rather than the spectroscopically confirmed ELGs from ELG_LOP that we use. Moreover, they apply some additional cuts to improve the purity of the target sample (intended to remove low-redshift interlopers, quasars, and faint or high-redshift ELGs where a good redshift cannot be obtained). As a result, their sample selection is somewhat different from ours, and it is thus unsurprising that they find a different value of the magnification bias.

5.3 Evolution bias

The evolution bias is computed using the comoving number density of galaxies as shown in Fig. 7. We use the measured \bar{n} from SV3 tabulated by the DESI survey.¹² Subsequently, we smooth the noisy measured $\bar{n}(z)$ using a smoothing spline. We verify that the fluctuations seen in $\bar{n}(z)$ are driven by cosmic variance due to the small area covered, by comparing to the

¹²<https://data.desi.lbl.gov/doc/releases/edr/vac/lss/>

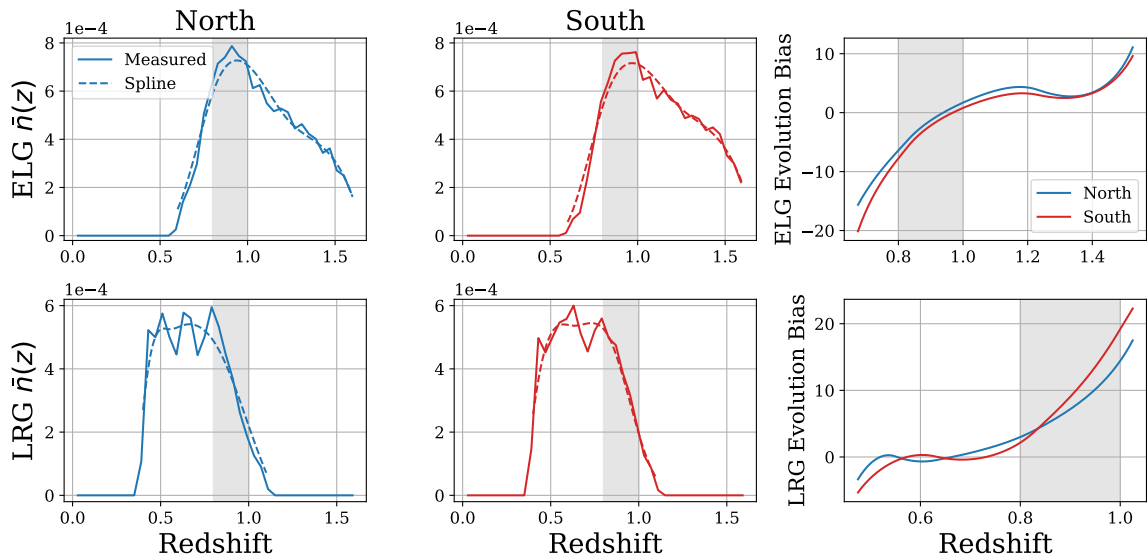


Figure 7: The left and middle columns show the comoving number density of the ELG and LRG samples as a function of redshift. The left column is from the North galaxy sample while the middle column is from the South galaxy sample. The right column shows the evolution bias for both the ELG and LRG samples computed from $\bar{n}(z)$ using Eq. (2.4). The grey rectangle highlights the redshift range of interest.

redshift distributions from the first two months of the DESI main survey as shown in Fig. 19 in [27]. The fluctuations in $\bar{n}(z)$ are smaller in this sample, as would be expected since it covers a much larger area. Averaging over the $0.8 < z < 1.0$ range and weighting by $\bar{n}(z)$, we find -1.2 and -2.1 for the North and South ELG sample and 8.1 and 10.2 for the North and South LRG sample.

To summarize the contributions of the various terms that multiply the velocity in Eq. 2.1 (which are grouped together in \mathcal{R}_v as defined in Eq. 2.2), we plot them together in Fig. 8. This shows that they are generally of similar magnitude, and there are significant cancellations between positive and negative terms.

6 Impact on two-point statistics

In Fig. 9 we show both the ELG auto-correlation and the ELG-LRG cross-correlation, in the redshift range of interest at $0.8 < z < 1.0$. We compute the dipole both with and without the Doppler bias. As expected, the impact of b_D on the ELG-LRG cross-correlation is much larger. Adding b_D only affects the ELG auto-correlation on very large scales, at $k < 0.03 h \text{ Mpc}^{-1}$. The impact of b_D on the cross-correlation is also scale-dependent, increasing the cross-correlation by 30% at $k < 0.1 h \text{ Mpc}^{-1}$ and 15–20% at $k > 0.3 h \text{ Mpc}^{-1}$. We also find a small impact of b_D on large-scales in the monopole P_0 and quadrupole P_2 : for the ELG auto-correlation, b_D shifts the monopole by 0.5% at $k = 0.01 h \text{ Mpc}^{-1}$ and the quadrupole by $\sim 2\%$, whereas for the ELG-LRG cross-correlation, b_D changes the monopole by 0.1% at $k = 0.01 h \text{ Mpc}^{-1}$ and the quadrupole by 2%. Due to the scale-dependence of the change, it is unlikely to affect cosmological parameter inference (i.e. measurements of $f\sigma_8$), but it could potentially affect f_{NL} constraints. However, the impact of b_D on the cross-correlation dipole

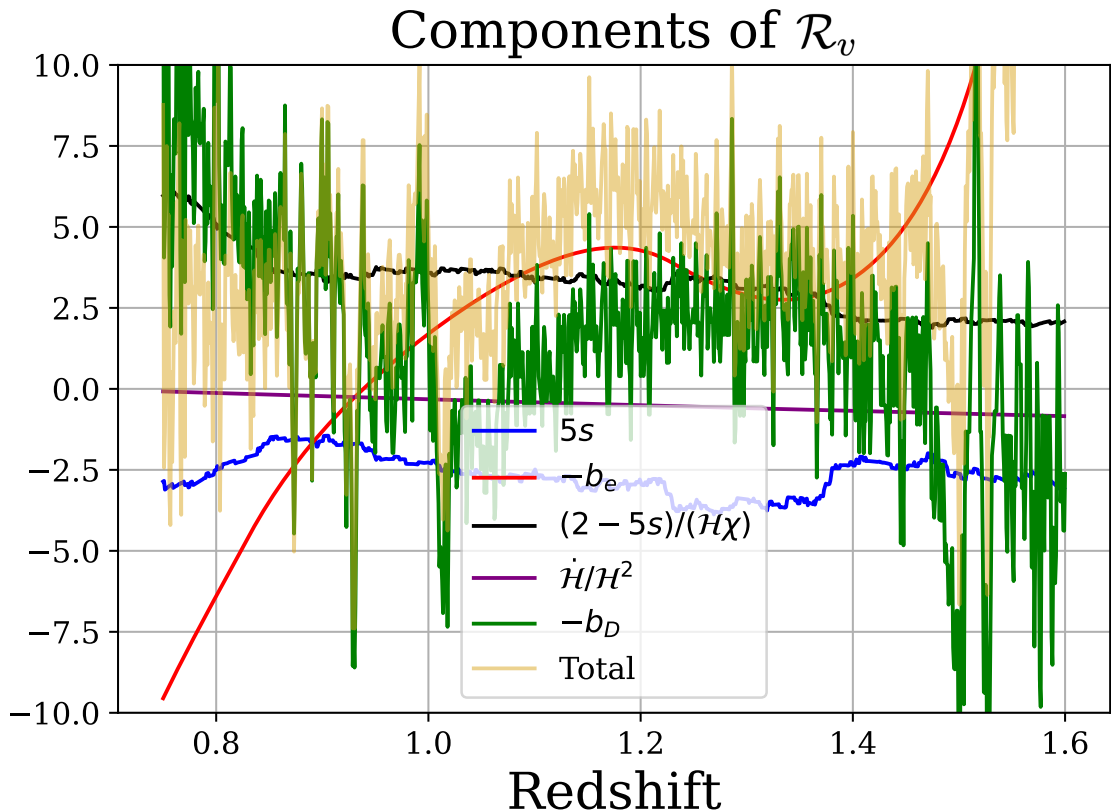


Figure 8: Components of \mathcal{R}_v , which quantifies the line-of-sight peculiar velocity modulation of galaxy density, in Eq. 2.7. The vertical axis is unlabeled because each of these components is unitless.

is considerably larger, and we will hereafter only consider its impact on $P_1(k)$, leaving its impact on the monopole and quadrupole to future work.

We performed a number of convergence checks to verify that the calculated power spectra are not affected by numerical issues. We found that the results were robust to varying GaPSE settings, aside from the `cut_first_n` and `cut_last_n` arguments. These parameters are necessary when using a window function, because the correlation function at very large scales drops to zero and therefore the FFTLog fails, leading to problematic oscillatory behavior. We found that cutting the first point and last three points of the correlation function removed the problematic oscillatory behavior for the majority of the power spectrum multipoles, but changing these parameters when making different power spectra is often necessary.

We then compute the signal-to-noise ratio of the difference between the dipole with b_D and without b_D

$$\left(\frac{S}{N}\right)^2 = \frac{1}{4\pi^2} V_{\text{survey}} \int_{k_{\text{min}}}^{k_{\text{max}}} dk k^2 \frac{[P_1^{b_D}(k) - P_1^{b_D=0}(k)]^2}{\sigma_{P_1}^2(k)} \quad (6.1)$$

where V_{survey} is the volume probed by a 14,000 deg² survey at $0.8 < z < 1.0$. We calculate the signal-to-noise separately for the North and South survey regions, since they have quite

different values for b_D ; we assume 5000 deg² in the North footprint (declination $> 30^\circ$) and 9000 deg² in the South.

For $\sigma_{P_1}(k)$, we use the flat-sky Gaussian covariance estimate from Eq. 7.8 in [4]:

$$\begin{aligned} \sigma_{P_1^{XY}}^2(k) = & -\frac{9}{10}P_1^{XY}(k)^2 - \frac{18}{35}P_1^{XY}(k)P_3(k) - \frac{23}{70}P_3^{XY}(k)^2 \\ & - \frac{20}{77}P_3^{XY}(k)P_5^{XY}(k) - \frac{59}{286}P_5^{XY}(k)^2 \\ & + \frac{3}{2\bar{n}_X}P_0^{YY}(k) + \frac{3}{2\bar{n}_Y}P_0^{XX}(k) + \frac{3}{2\bar{n}_X\bar{n}_Y} \\ & + \frac{3}{5\bar{n}_X}P_2^{YY}(k) + \frac{3}{5\bar{n}_Y}P_2^{XX}(k) \quad (6.2) \end{aligned}$$

This analytic calculation for the dipole covariance neglects window function effects, although we do include their contributions to the multipoles.

We find a cumulative expected signal-to-noise of 4.5σ for the ELG-LRG dipole induced by b_D (Fig. 10), with the South detection (4σ) considerably larger than the North (2σ). This difference is a combination of the larger b_D in the South as well as its larger survey volume. The signal-to-noise is dominated by large, linear scales. It is only reduced 5% if we use $k_{\max} = 0.2 h \text{ Mpc}^{-1}$, and 20% if we use $k_{\max} = 0.1 h \text{ Mpc}^{-1}$. On the other hand, if we set $k_{\min} = 0.02 h \text{ Mpc}^{-1}$, the signal-to-noise is reduced 10%, and if we set $k_{\min} = 0.05 h \text{ Mpc}^{-1}$, the signal-to-noise is reduced 30%.

This suggests that the Doppler bias could have a measurable impact on the ELG-LRG dipole measured by DESI at $0.8 < z < 1$. We note that there is some systematic uncertainty in our b_D estimates, due to potential incompleteness in the parent ELG sample that we created from DESI SV1. Nevertheless, it is clear that excluding b_D could measurably change theory predictions for $P_1(k)$, potentially biasing efforts to use the dipole to measure cosmological parameters or test gravity. At 4.5σ , the impact of b_D on the DESI ELG-LRG dipole is larger than the 1.6σ detection significance for the same cross-correlation forecasted in [4], which considered the $z \sim 0.3$ DESI BGS sample as a more promising target for the dipole. Indeed, we find a considerably higher total detection significance of the ELG-LRG $P_1(k)$ than [4], 12σ in the North and 19σ in the South. However, there are several differences between our setup and theirs, which account for this discrepancy. They assume $s = 0$ and $b_e = 0$, whereas we use the values in Table 1. If we set $b_D = 0$ and $b_e = 0$ for both tracers, we get 4.9 and 6.7σ , and if we also set $s = 0$, we get 5.7 and 7.6σ (the detection significance is slightly higher because s is < 0.4 , i.e. it has a negative impact on the overall signal). Also, the dipole signal in [4] is flat-sky only, i.e. they do not count the Newtonian (wide-angle) contribution to the signal as they are only interested in the detectability of the relativistic terms. If we also remove the auto-Newton term from the dipole, we get a detection significance of 2.2 and 2.9σ . This is still slightly higher than [4], but the redshift range considered is different, and, moreover, whether we use the linear power spectrum only (as in this work) or include higher-order terms and an EFT velocity dispersion (as in that work), makes a $\sim 30\%$ difference in the signal-to-noise for BGS (their Fig. 10). Overall, we conclude that our results are broadly consistent with those of [4], if the same assumptions are made about the galaxy bias parameters. Furthermore, our results suggest that b_D could also have a substantial impact on the DESI BGS sample that they study—although note that we expect b_D to be smaller for BGS since it is not as emission line dominated as the ELGs.

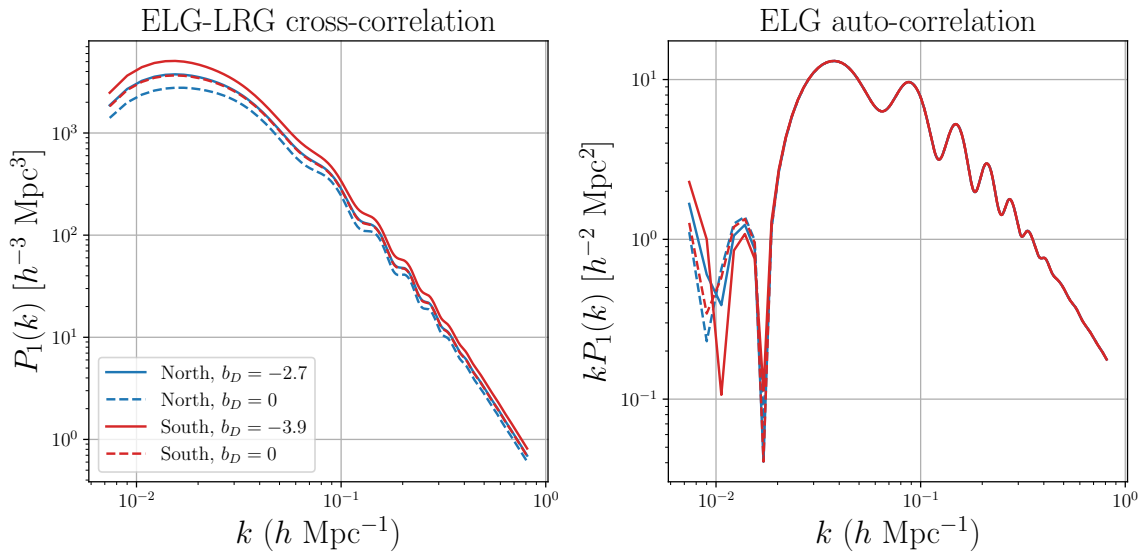


Figure 9: Dipole of the power spectrum with and without Doppler bias, using $b_D = -3.9$ (South) and -2.7 (North). The left panel shows the ELG-LRG cross-correlation, and the right panel shows the ELG autocorrelation, in both cases at $0.8 < z < 1$. Note that the near complete overlap of the North $b_D \neq 0$ cross-correlation with the South $b_D = 0$ cross-correlation is just a coincidence.

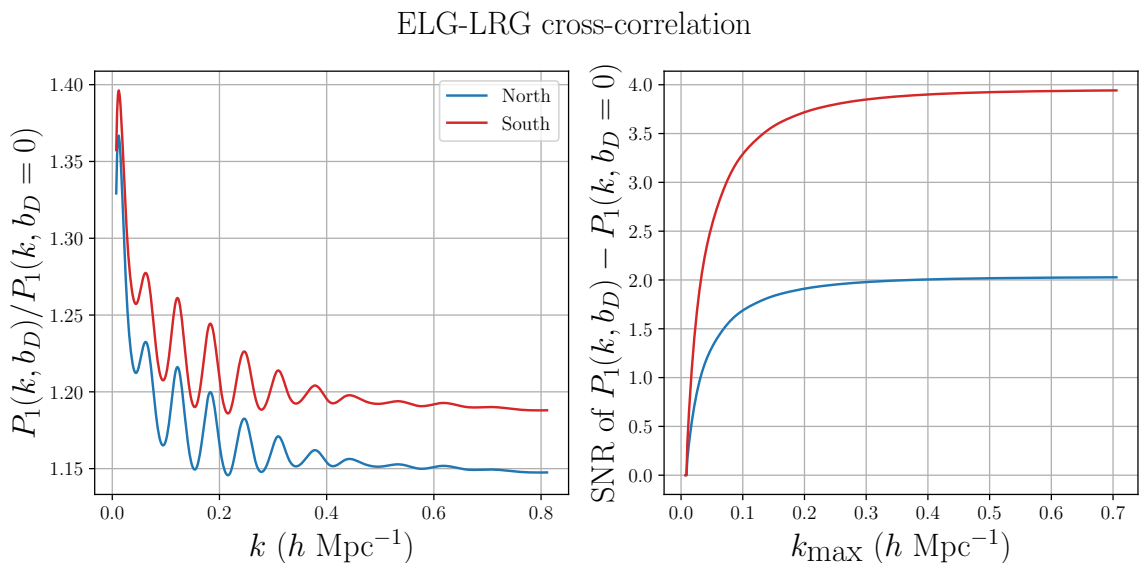


Figure 10: *Left:* fractional impact of the Doppler bias: ratio of the ELG-LRG cross-correlation dipole with b_D , to the dipole with $b_D = 0$, in a bin at $0.8 < z < 1$. *Right:* Signal-to-noise ratio of the difference in $P_1(k)$ between the default values of b_D (-2.7 in the North and -3.9 in the South) and $b_D = 0$, as a function of the minimum scale used k_{max} .

7 Conclusion and Future Prospects

By shifting emission lines into and out of filter bandpasses, peculiar velocities can have a large impact on the target selection of Emission Line Galaxies in spectroscopic surveys, which uses galaxy colors in broad-band imaging. This leads to an additional contribution to the evolution bias, which we name the Doppler bias, b_D . This Doppler bias contributes to relativistic terms in the galaxy power spectrum. We measure the Doppler bias for DESI Emission Line Galaxies (ELGs), using an extended sample of ELGs from DESI’s early Survey Validation (SV1) on which we can Doppler shift the galaxies and measure the impact on the main DESI ELG selection. The Doppler bias can be quite large in narrow ranges in redshift, although the overall impact on a broad redshift bin that would be used for galaxy clustering measurements is modest. The Doppler bias depends on the detailed properties of the filters used in the underlying imaging surveys. For DESI, it is thus different between the North and South regions, where the underlying imaging surveys (and thus the filter bandpasses) are different. We quantify the impact of the Doppler bias on galaxy clustering using the code GaPSE. The largest impact of peculiar velocities is on the imaginary part of the power spectrum for cross-correlations between two tracers of different bias. This translates into the clustering dipole $P_1(k)$, since the Doppler bias breaks inversion symmetry $\vec{r} \rightarrow -\vec{r}$. DESI LRGs offer an ideal sample for cross-correlation with ELGs in the redshift range of interest, $0.8 < z < 1.0$, with $\Delta b \sim 0.7$. We estimate that the Doppler bias contribution changes the ELG-LRG dipole at a 4.5σ level (4σ in the South and 2σ in the North, where the estimated Doppler bias is smaller due to differences in the filter bandpasses). While this estimate is affected by systematic uncertainties in the Doppler bias measurement due to potential incompleteness in the SV1 parent sample of ELGs, it suggests that the Doppler bias will have a measurable impact on the multi-tracer dipole and could therefore affect cosmological measurements or tests of gravity based on the dipole. On the other hand the impact of b_D is much more moderate on the ELG autocorrelation, or the monopole and quadrupole in either the autocorrelation or ELG-LRG cross-correlation. As rapidly improving datasets will soon allow us to detect the multi-tracer dipole for the first time, our work motivates the inclusion of the Doppler bias in theoretical calculations and modelling that already includes the evolution bias. While we have measured the Doppler bias for Emission Line Galaxies where we expect the effect to be especially large, it should also exist for other samples of galaxies, such as the DESI Bright Galaxy Sample (BGS) that is considered the most promising to search for relativistic effects in the dipole [4]. Furthermore, rather than attempting to measure b_D from first principles, one could instead use measurements of the dipole to constrain the true value of the Doppler bias, similar to the proposal of [85] for the evolution bias.

Another interesting future prospect would be exploring the impact of the Doppler bias on parity violation in the galaxy trispectrum or four-point function, as an explanation for the claimed detections of [86, 87].¹³ As explored in [90], relativistic terms can contribute to parity violation in the trispectrum, and our Doppler bias would enhance these relativistic terms. The magnitude of the parity violation due to the Doppler bias would be highly sample dependent, but is nevertheless crucial to constrain.

Additionally, the dipole measured from the distribution of distant quasars seems to be anomalously large compared to the dipole in the CMB [91, 92]. The Doppler bias could contribute an extra term to the classical Ellis-Baldwin formula [93] and thus potentially explain

¹³But see [88, 89] for arguments that the parity-violating signal could be due to residual systematics in the data or simulations used.

the discrepancy. Further research is necessary to quantify the impact of the Doppler bias in these cases. Further into the future, Emission Line Galaxies will become increasingly important for large-scale structure measurements, as surveys push to high redshift where galaxies become increasingly faint and strong emission lines offer the best prospects for obtaining redshifts. Euclid will target H α emitters at $z \sim 0.9$ – 1.8 [30]; similarly, WFIRST plans to observe both H α emitters and [OIII] galaxies [31]; and, finally, Stage 5 spectroscopic surveys will target Lyman alpha emitters as a key tracer of matter at $z > 2$ [32, 33]. As a result, understanding the impact of peculiar velocities on galaxy selection will remain important for precision modelling of large-scale galaxy clustering and testing gravity via relativistic effects.

Lastly, with the proper engineering of band pass filters, and careful forethought about galaxy targeting, the Doppler bias could realistically be used to probe the radial peculiar velocity field in certain redshifts, though a high degree of precision would be needed in observation, sample completeness, and analysis to usefully probe the large-scale velocity field.

8 Acknowledgements

We thank Stephen Bailey, Marco Bonici, Emanuele Castorina, Enea Di Dio, Matt Johnson, Tanveer Karim, Francisco-Shu Kitaura, Pritha Paul, Will Percival, Hanne Silverans, Licia Verde, Cheng Zhao, and Rongpu Zhou and for useful correspondence, suggestions, and encouragement. We especially thank Dustin Lang for many fruitful discussions throughout the course of this work.

This work is supported by the Natural Sciences and Engineering Research Council of Canada, the University of Waterloo, and the Perimeter Institute for Theoretical Physics. Research at Perimeter Institute is supported in part by the Government of Canada through the Department of Innovation, Science, and Economic Development of Canada and by the Province of Ontario through the Ministry of Colleges and Universities.

AK was supported as a CITA National Fellow by the Natural Sciences and Engineering Research Council of Canada (NSERC), funding reference #DIS-2022-568580.

References

- [1] N. Kaiser, *Clustering in real space and in redshift space*, *Mon. Not. R. Astron. Soc.* **227** (1987) 1.
- [2] E. Di Dio and U. Seljak, *The relativistic dipole and gravitational redshift on LSS*, *JCAP* **2019** (2019) 050 [1811.03054].
- [3] E. Di Dio and F. Beutler, *The relativistic galaxy number counts in the weak field approximation*, *JCAP* **2020** (2020) 058 [2004.07916].
- [4] F. Beutler and E. Di Dio, *Modeling relativistic contributions to the halo power spectrum dipole*, *JCAP* **2020** (2020) 048 [2004.08014].
- [5] E. Castorina and E. Di Dio, *The observed galaxy power spectrum in general relativity*, *Journal of Cosmology and Astroparticle Physics* **2022** (2022) 061.
- [6] S. Saga, A. Taruya, Y. Rasera and M.-A. Breton, *Cosmological test of local position invariance from the asymmetric galaxy clustering*, *Mon. Not. R. Astron. Soc.* **524** (2023) 4472 [2112.07727].
- [7] J. Beltrán Jiménez, E. Di Dio and D. Figueruelo, *A smoking gun from the power spectrum dipole for elastic interactions in the dark sector*, *JCAP* **2023** (2023) 088 [2212.08617].

- [8] O. Umeh, K. Koyama and R. Crittenden, *Testing the equivalence principle on cosmological scales using the odd multipoles of galaxy cross-power spectrum and bispectrum*, *JCAP* **2021** (2021) 049 [[2011.05876](#)].
- [9] C. Bonvin and P. Fleury, *Testing the equivalence principle on cosmological scales*, *JCAP* **2018** (2018) 061 [[1803.02771](#)].
- [10] C. Bonvin, F. Oliveira Franco and P. Fleury, *A null test of the equivalence principle using relativistic effects in galaxy surveys*, *JCAP* **2020** (2020) 004 [[2004.06457](#)].
- [11] S. Camera, M. G. Santos and R. Maartens, *Probing primordial non-Gaussianity with SKA galaxy redshift surveys: a fully relativistic analysis*, *Mon. Not. R. Astron. Soc.* **448** (2015) 1035 [[1409.8286](#)].
- [12] D. Alonso, P. Bull, P. G. Ferreira, R. Maartens and M. G. Santos, *Ultra-large-scale Cosmology in Next-generation Experiments with Single Tracers*, *Astrop. J.* **814** (2015) 145 [[1505.07596](#)].
- [13] J. Fonseca, S. Camera, M. G. Santos and R. Maartens, *Hunting Down Horizon-scale Effects with Multi-wavelength Surveys*, *Astrophys. J. Lett.* **812** (2015) L22 [[1507.04605](#)].
- [14] A. Raccañelli, F. Montanari, D. Bertacca, O. Doré and R. Durrer, *Cosmological measurements with general relativistic galaxy correlations*, *JCAP* **2016** (2016) 009 [[1505.06179](#)].
- [15] J. Yoo, N. Hamaus, U. Seljak and M. Zaldarriaga, *Going beyond the Kaiser redshift-space distortion formula: A full general relativistic account of the effects and their detectability in galaxy clustering*, *Phys. Rev. D* **86** (2012) 063514 [[1109.0998](#)].
- [16] M. S. Wang, F. Beutler and D. Bacon, *Impact of relativistic effects on the primordial non-Gaussianity signature in the large-scale clustering of quasars*, *Mon. Not. R. Astron. Soc.* **499** (2020) 2598 [[2007.01802](#)].
- [17] P. McDonald, *Gravitational redshift and other redshift-space distortions of the imaginary part of the power spectrum*, *Journal of Cosmology and Astroparticle Physics* **2009** (2009) 026.
- [18] C. Bonvin, L. Hui and E. Gaztañaga, *Asymmetric galaxy correlation functions*, *Phys. Rev. D* **89** (2014) 083535 [[1309.1321](#)].
- [19] V. Desjacques, D. Jeong and F. Schmidt, *Large-scale galaxy bias*, *Phys. Rep.* **733** (2018) 1 [[1611.09787](#)].
- [20] L. Castiblanco, R. Gannouji, J. Noreña and C. Stahl, *Relativistic cosmological large scale structures at one-loop*, *JCAP* **2019** (2019) 030 [[1811.05452](#)].
- [21] M. Noorikuhani and R. Scoccimarro, *Wide-angle and relativistic effects in Fourier-space clustering statistics*, *Phys. Rev. D* **107** (2023) 083528 [[2207.12383](#)].
- [22] M. Bartelmann and P. Schneider, *Weak gravitational lensing*, *Phys. Rep.* **340** (2001) 291 [[astro-ph/9912508](#)].
- [23] L. Wenzl, S.-F. Chen and R. Bean, *Magnification bias estimators for realistic surveys: an application to the BOSS survey*, *Mon. Not. R. Astron. Soc.* **527** (2024) 1760 [[2308.05892](#)].
- [24] J. Elvin-Poole, N. MacCrann, S. Everett, J. Prat, E. S. Rykoff, J. De Vicente et al., *Dark Energy Survey Year 3 results: magnification modelling and impact on cosmological constraints from galaxy clustering and galaxy-galaxy lensing*, *Mon. Not. R. Astron. Soc.* **523** (2023) 3649 [[2209.09782](#)].
- [25] R. Maartens, J. Fonseca, S. Camera, S. Jolicœur, J.-A. Viljoen and C. Clarkson, *Magnification and evolution biases in large-scale structure surveys*, *JCAP* **2021** (2021) 009 [[2107.13401](#)].
- [26] DESI Collaboration, A. Aghamousa, J. Aguilar, S. Ahlen, S. Alam, L. E. Allen et al., *The DESI Experiment Part I: Science, Targeting, and Survey Design*, *arXiv e-prints* (2016) [arXiv:1611.00036](#) [[1611.00036](#)].

- [27] Raichoor et al., in prep.
- [28] S. Alam, R. A. C. Croft, S. Ho, H. Zhu and E. Giusarma, *Relativistic effects on galaxy redshift samples due to target selection*, *Mon. Not. R. Astron. Soc.* **471** (2017) 2077 [1709.07856].
- [29] F. Beutler, E. Castorina and P. Zhang, *Interpreting measurements of the anisotropic galaxy power spectrum*, *Journal of Cosmology and Astroparticle Physics* **2019** (2019) 040–040.
- [30] R. Laureijs, J. Amiaux, S. Arduini, J. L. Auguères, J. Brinchmann, R. Cole et al., *Euclid definition study report*, **1110.3193**.
- [31] D. Spergel, N. Gehrels, C. Baltay, D. Bennett, J. Breckinridge, M. Donahue et al., *Wide-Field Infrared Survey Telescope-Astrophysics Focused Telescope Assets WFIRST-AFTA 2015 Report*, *arXiv e-prints* (2015) arXiv:1503.03757 [1503.03757].
- [32] D. J. Schlegel, S. Ferraro, G. Aldering, C. Baltay, S. BenZvi, R. Besuner et al., *A Spectroscopic Road Map for Cosmic Frontier: DESI, DESI-II, Stage-5*, *arXiv e-prints* (2022) arXiv:2209.03585 [2209.03585].
- [33] D. J. Schlegel, J. A. Kollmeier, G. Aldering, S. Bailey, C. Baltay, C. Bebek et al., *The MegaMapper: A Stage-5 Spectroscopic Instrument Concept for the Study of Inflation and Dark Energy*, *arXiv e-prints* (2022) arXiv:2209.04322 [2209.04322].
- [34] M. Foglieni, M. Pantiri, E. Di Dio and E. Castorina, *The large scale limit of the observed galaxy power spectrum*, *arXiv e-prints* (2023) arXiv:2303.03142 [2303.03142].
- [35] K. Yamamoto, M. Nakamichi, A. Kamino, B. A. Bassett and H. Nishioka, *A Measurement of the Quadrupole Power Spectrum in the Clustering of the 2dF QSO Survey*, *Pub. of ASJ* **58** (2006) 93 [astro-ph/0505115].
- [36] D. Bianchi, H. Gil-Marín, R. Ruggeri and W. J. Percival, *Measuring line-of-sight-dependent Fourier-space clustering using FFTs*, *Mon. Not. R. Astron. Soc.* **453** (2015) L11 [1505.05341].
- [37] R. Scoccimarro, *Fast estimators for redshift-space clustering*, *Phys. Rev. D* **92** (2015) 083532 [1506.02729].
- [38] Z. Slepian and D. J. Eisenstein, *Accelerating the two-point and three-point galaxy correlation functions using Fourier transforms*, *Mon. Not. R. Astron. Soc.* **455** (2016) L31 [1506.04746].
- [39] N. Hand, Y. Li, Z. Slepian and U. Seljak, *An optimal FFT-based anisotropic power spectrum estimator*, *JCAP* **2017** (2017) 002 [1704.02357].
- [40] F. Beutler and P. McDonald, *Unified galaxy power spectrum measurements from 6dFGS, BOSS, and eBOSS*, *JCAP* **2021** (2021) 031 [2106.06324].
- [41] A. S. Szalay, T. Matsubara and S. D. Landy, *Redshift-Space Distortions of the Correlation Function in Wide-Angle Galaxy Surveys*, *Astrophys. J. Lett.* **498** (1998) L1 [astro-ph/9712007].
- [42] I. Szapudi, *Wide-Angle Redshift Distortions Revisited*, *Astrop. J.* **614** (2004) 51 [astro-ph/0404477].
- [43] P. Pápai and I. Szapudi, *Non-perturbative effects of geometry in wide-angle redshift distortions*, *Mon. Not. R. Astron. Soc.* **389** (2008) 292 [0802.2940].
- [44] A. Raccanelli, L. Samushia and W. J. Percival, *Simulating redshift-space distortions for galaxy pairs with wide angular separation*, *Mon. Not. R. Astron. Soc.* **409** (2010) 1525 [1006.1652].
- [45] J. Yoo and U. Seljak, *Wide-angle effects in future galaxy surveys*, *Mon. Not. R. Astron. Soc.* **447** (2015) 1789 [1308.1093].
- [46] E. Castorina and M. White, *Beyond the plane-parallel approximation for redshift surveys*, *Mon. Not. R. Astron. Soc.* **476** (2018) 4403 [1709.09730].

- [47] E. Castorina and M. White, *The Zeldovich approximation and wide-angle redshift-space distortions*, *Mon. Not. R. Astron. Soc.* **479** (2018) 741 [1803.08185].
- [48] P. Reimberg, F. Bernardeau and C. Pitrou, *Redshift-space distortions with wide angular separations*, *JCAP* **2016** (2016) 048 [1506.06596].
- [49] M. Pantiri, M. Foglieni, E. Di Dio and E. Castorina, *The power spectrum of luminosity distance fluctuations in General Relativity*, *arXiv e-prints* (2024) arXiv:2407.01486 [2407.01486].
- [50] DESI Collaboration, A. G. Adame, J. Aguilar, S. Ahlen, S. Alam, G. Aldering et al., *Validation of the Scientific Program for the Dark Energy Spectroscopic Instrument*, *arXiv e-prints* (2023) arXiv:2306.06307 [2306.06307].
- [51] N. Aghanim, Y. Akrami, M. Ashdown, J. Aumont, C. Baccigalupi, M. Ballardini et al., *Planck2018 results: Vi. cosmological parameters*, *Astronomy & Astrophysics* **641** (2020) A6.
- [52] DESI Collaboration, A. G. Adame, J. Aguilar, S. Ahlen, S. Alam, G. Aldering et al., *The Early Data Release of the Dark Energy Spectroscopic Instrument*, *arXiv e-prints* (2023) arXiv:2306.06308 [2306.06308].
- [53] DESI Collaboration, A. Aghamousa, J. Aguilar, S. Ahlen, S. Alam, L. E. Allen et al., *The DESI Experiment Part II: Instrument Design*, *arXiv e-prints* (2016) arXiv:1611.00037 [1611.00037].
- [54] B. Abareschi, J. Aguilar, S. Ahlen, S. Alam, D. M. Alexander, R. Alfarsy et al., *Overview of the Instrumentation for the Dark Energy Spectroscopic Instrument*, *arXiv e-prints* (2022) arXiv:2205.10939 [2205.10939].
- [55] E. F. Schlafly, D. Kirkby, D. J. Schlegel, A. D. Myers, A. Raichoor, K. Dawson et al., *Survey Operations for the Dark Energy Spectroscopic Instrument*, *Astron. J.* **166** (2023) 259 [2306.06309].
- [56] J. H. Silber, P. Fagrelus, K. Fanning, M. Schubnell, J. N. Aguilar, S. Ahlen et al., *The Robotic Multiobject Focal Plane System of the Dark Energy Spectroscopic Instrument (DESI)*, *Astron. J.* **165** (2023) 9 [2205.09014].
- [57] T. N. Miller, P. Doel, G. Gutierrez, R. Besuner, D. Brooks, G. Gallo et al., *The Optical Corrector for the Dark Energy Spectroscopic Instrument*, *arXiv e-prints* (2023) arXiv:2306.06310 [2306.06310].
- [58] J. Guy, S. Bailey, A. Kremin, S. Alam, D. M. Alexander, C. Allende Prieto et al., *The Spectroscopic Data Processing Pipeline for the Dark Energy Spectroscopic Instrument*, *Astron. J.* **165** (2023) 144 [2209.14482].
- [59] Bailey et al., *in preparation* (2024) .
- [60] A. D. Myers, J. Moustakas, S. Bailey, B. A. Weaver, A. P. Cooper, J. E. Forero-Romero et al., *The Target-selection Pipeline for the Dark Energy Spectroscopic Instrument*, *Astron. J.* **165** (2023) 50 [2208.08518].
- [61] D. Bianchi, A. Burden, W. J. Percival, D. Brooks, R. N. Cahn, J. E. Forero-Romero et al., *Unbiased clustering estimates with the DESI fibre assignment*, *Mon. Not. R. Astron. Soc.* **481** (2018) 2338 [1805.00951].
- [62] D. Bianchi and W. J. Percival, *Unbiased clustering estimation in the presence of missing observations*, *Mon. Not. R. Astron. Soc.* **472** (2017) 1106 [1703.02070].
- [63] C. Hahn, R. Scoccimarro, M. R. Blanton, J. L. Tinker and S. A. Rodríguez-Torres, *The Effect of Fiber Collisions on the Galaxy Power Spectrum Multipoles*, *Mon. Not. R. Astron. Soc.* **467** (2017) 1940 [1609.01714].
- [64] A. Smith, J.-h. He, S. Cole, L. Stothert, P. Norberg, C. Baugh et al., *Correcting for fibre assignment incompleteness in the DESI Bright Galaxy Survey*, *Mon. Not. R. Astron. Soc.* **484** (2019) 1285 [1809.07355].

- [65] L. Pinol, R. N. Cahn, N. Hand, U. Seljak and M. White, *Imprint of DESI fiber assignment on the anisotropic power spectrum of emission line galaxies*, *JCAP* **2017** (2017) 008 [[1611.05007](#)].
- [66] M. Pinon, A. de Mattia, P. McDonald, E. Burtin, V. Ruhlmann-Kleider, M. White et al., *Mitigation of DESI fiber assignment incompleteness effect on two-point clustering with small angular scale truncated estimators*, *arXiv e-prints* (2024) [arXiv:2406.04804](#) [[2406.04804](#)].
- [67] D. Schlegel, A. Dey, D. Herrera, S. Juneau, M. Landriau, D. Lang et al., *DESI Legacy Imaging Surveys Data Release 9*, *Bulletin of the AAS* **53** (2021) .
- [68] H. Zou, J. Gao, X. Zhou and X. Kong, *Photometric redshifts and stellar masses for galaxies from the desi legacy imaging surveys*, *The Astrophysical Journal Supplement Series* **242** (2019) 8.
- [69] B. Flaugher, H. T. Diehl, K. Honscheid, T. M. C. Abbott, O. Alvarez, R. Angstadt et al., *The dark energy camera*, *The Astronomical Journal* **150** (2015) 150.
- [70] A. Dey, D. J. Schlegel, D. Lang, R. Blum, K. Burleigh, X. Fan et al., *Overview of the desi legacy imaging surveys*, *The Astronomical Journal* **157** (2019) 168.
- [71] D. Lang, D. Hogg and D. Mykytyn, *The Tractor: Probabilistic astronomical source detection and measurement*, 2016.
- [72] D. J. Schlegel, D. P. Finkbeiner and M. Davis, *Maps of Dust Infrared Emission for Use in Estimation of Reddening and Cosmic Microwave Background Radiation Foregrounds*, *Astrop. J.* **500** (1998) 525 [[astro-ph/9710327](#)].
- [73] R. Zhou, J. Guy, S. E. Koposov, E. F. Schlafly, D. Schlegel, J. Aguilar et al., *Stellar reddening map from DESI imaging and spectroscopy*, *arXiv e-prints* (2024) [arXiv:2409.05140](#) [[2409.05140](#)].
- [74] E. Chaussidon, C. Yèche, N. Palanque-Delabrouille, D. M. Alexander, J. Yang, S. Ahlen et al., *Target selection and validation of desi quasars*, *The Astrophysical Journal* **944** (2023) 107.
- [75] J. Yu, A. J. Ross, A. Rocher, O. Alves, A. de Mattia, D. Forero-Sánchez et al., *ELG Spectroscopic Systematics Analysis of the DESI Data Release 1*, *arXiv e-prints* (2024) [arXiv:2405.16657](#) [[2405.16657](#)].
- [76] D. Kirkby, T. Robitaille, B. A. Weaver, Moustakas, E. Tollerud, M. Droettboom et al., *desihub/speclite: Bug fix release: General clean- up prior to refactoring package infrastructure*, Aug., 2024. [10.5281/zenodo.13225530](#).
- [77] S. Samuroff, J. Blazek, M. A. Troxel, N. MacCrann, E. Krause, C. D. Leonard et al., *Dark Energy Survey Year 1 results: constraints on intrinsic alignments and their colour dependence from galaxy clustering and weak lensing*, *Mon. Not. R. Astron. Soc.* **489** (2019) 5453 [[1811.06989](#)].
- [78] A. J. Mead, S. Brieden, T. Tröster and C. Heymans, *HMCODE-2020: improved modelling of non-linear cosmological power spectra with baryonic feedback*, *Mon. Not. R. Astron. Soc.* **502** (2021) 1401 [[2009.01858](#)].
- [79] A. Lewis, A. Challinor and A. Lasenby, *Efficient Computation of CMB anisotropies in closed FRW models*, *The Astrophysical Journal* **538** (1999) 473 [[9911177v2](#)].
- [80] C. Howlett, A. Lewis, A. Hall and A. Challinor, *CMB power spectrum parameter degeneracies in the era of precision cosmology*, *Journal of Cosmology and Astroparticle Physics* **2012** (2012) [[1201.3654v2](#)].
- [81] Hagen et al., *in preparation* (2024) .
- [82] M. White, R. Zhou, J. DeRose, S. Ferraro, S.-F. Chen, N. Kokron et al., *Cosmological constraints from the tomographic cross-correlation of DESI Luminous Red Galaxies and Planck CMB lensing*, *JCAP* **2022** (2022) 007 [[2111.09898](#)].

- [83] R. Zhou, S. Ferraro, M. White, J. DeRose, N. Sailer, J. Aguilar et al., *DESI luminous red galaxy samples for cross-correlations*, *JCAP* **2023** (2023) 097 [[2309.06443](#)].
- [84] T. Karim, S. Singh, M. Rezaie, D. Eisenstein, B. Hadzhiyska, J. S. Speagle et al., *Measuring σ_8 using DESI Legacy Imaging Surveys Emission-Line Galaxies and Planck CMB Lensing and the Impact of Dust on Parameter Inferenc*, *arXiv e-prints* (2024) [arXiv:2408.15909](#) [[2408.15909](#)].
- [85] D. Sobral-Blanco, C. Bonvin, C. Clarkson and R. Maartens, *Using relativistic effects in large-scale structure to constrain astrophysical properties of galaxy populations*, *arXiv e-prints* (2024) [arXiv:2406.19908](#) [[2406.19908](#)].
- [86] J. Hou, Z. Slepian and R. N. Cahn, *Measurement of parity-odd modes in the large-scale 4-point correlation function of Sloan Digital Sky Survey Baryon Oscillation Spectroscopic Survey twelfth data release CMASS and LOWZ galaxies*, *Mon. Not. R. Astron. Soc.* **522** (2023) 5701 [[2206.03625](#)].
- [87] O. H. E. Philcox, *Probing parity violation with the four-point correlation function of BOSS galaxies*, *Phys. Rev. D* **106** (2022) 063501 [[arXiv:2206.04227](#)].
- [88] O. H. E. Philcox and J. Ereza, *Could Sample Variance be Responsible for the Parity-Violating Signal Seen in the BOSS Galaxy Survey?*, [2401.09523](#).
- [89] A. Krolewski, S. May, K. Smith and H. Hopkins, *No evidence for parity violation in BOSS*, *JCAP* **2024** (2024) 044 [[2407.03397](#)].
- [90] P. Paul, C. Clarkson and R. Maartens, *Apparent parity violation in the observed galaxy trispectrum*, [2402.16478](#).
- [91] N. J. Secrest, S. von Hausegger, M. Rameez, R. Mohayaee and S. Sarkar, *A challenge to the standard cosmological model*, *The Astrophysical Journal Letters* **937** (2022) L31.
- [92] M. Rameez, R. Mohayaee, S. Sarkar and J. Colin, *The dipole anisotropy of allwise galaxies*, *Monthly Notices of the Royal Astronomical Society* **477** (2018) 1772–1781.
- [93] G. F. R. Ellis and J. E. Baldwin, *On the expected anisotropy of radio source counts*, *Mon. Not. R. Astron. Soc.* **206** (1984) 377.